3-D multiparameter full-waveform inversion for ocean-bottom seismic data using an efficient fluid–solid coupled spectral-element solver

Jian Cao, Romain Brossier, Andrzej Górszczyk, Ludovic Métivier, Jean Virieux

Geophysical Journal International

Geophys. J. Int. (2022) **229,** 671–703
Advance Access publication 2021 November 27
GJI Seismology

https://doi.org/10.1093/gji/ggab484

3-D multiparameter full-waveform inversion for ocean-bottom seismic data using an efficient fluid–solid coupled spectral-element solver

Jian Cao [1], Romain Brossier,[1] Andrzej Górszczyk [1,3] Ludovic Métivier[1,2] and Jean Virieux[1]

[1] *Univ. Grenoble Alpes, ISTerre, Grenoble F-38000, France. E-mail: jian.cao@univ-grenoble-alpes.fr*
[2] *Univ. Grenoble Alpes, CNRS, LJK, Grenoble F-38000, France*
[3] *Institute of Geophysics, Polish Academy of Sciences, Warsaw, Poland*

Accepted 2021 November 25. Received 2021 November 10; in original form 2021 May 19

SUMMARY

Ocean-bottom seismic acquisition systems deployed on the seabed give access to three-component geophone data and hydrophone data. Compared with conventional streamer acquisitions, the separation of sources and receivers makes it possible to increase the maximum offset and azimuth coverage for improving the illumination at depth. Furthermore, the three-component geophones naturally capture elastic wave propagation effects. While this information is mostly overlooked up to now, reconstructing jointly *P*- and *S*-wave velocities would significantly improve the subsurface characterization. To achieve a 3-D high-resolution multiparameter reconstruction, we design an efficient 3-D fluid–solid coupled full waveform modelling and inversion engine. In this engine, fluid and solid domains are divided explicitly and handled with the acoustic and elastic wave equations, respectively. The numerical implementation is based on a time-domain spectral-element method (SEM) with a flexible 3-D Cartesian-based hexahedral mesh, which contributes to an accurate coupling of the acoustic and elastic wave equations and high computational efficiency through domain-decomposition based parallelization. We select the best acoustic–elastic coupled formulations among 4 possibilities with criteria based on numerical accuracy and implementation efficiency. Moreover, we propose a specific hybrid approach for the misfit gradient building so as to use a similar modelling solver for both forward and adjoint simulations. Synthetic case studies on a 3-D extended Marmousi-II model and a 3-D deep-water crustal-scale model illustrate how our modelling and inversion engine can efficiently extract information from ocean-bottom seismic data to simultaneously reconstruct both *P*- and *S*-wave velocities within a full waveform inversion framework.

Key words: Inverse theory; Numerical modelling; Waveform inversion; Computational seismology.

1 INTRODUCTION

In offshore surveys, ocean-bottom seismic acquisition (either OBC—ocean-bottom cables or OBN—ocean-bottom nodes) is emerging as a mainstream exploration technique. It has been widely used not only in the oil and gas industry for imaging quality enhancement under complex overburdens (such as salt bodies), but also in the field of regional scale seismology for deep target reconstruction owing to its turning waves recording (Operto *et al.* 2006; Górszczyk *et al.* 2017). Generally speaking, ocean-bottom acquisition mainly has the following two advantages when compared with conventional streamer acquisitions: (1) separating sources from receivers to achieve a wide-azimuth coverage and long source–receiver distance for improving the illumination at depth, (2) providing more subsurface information through a richer amount of data with hydrophones in the water and three-component (3C) geophones on the seabed which can directly record elastic effects for *S*-wave velocity reconstruction (Maver 2011; Walker 2020).

Full waveform inversion (FWI) is a powerful technique to extract high-resolution quantitative physical parameters of the subsurface by fitting the full information of seismic data (Lailly 1983; Tarantola 1984; Virieux & Operto 2009; Virieux *et al.* 2017). In marine environments, most FWI studies are developed in the acoustic approximation (with or without anisotropy and attenuation) only using the pressure data

recorded in the water (Sirgue *et al.* 2010; Morgan *et al.* 2013; Prieux *et al.* 2013a; Operto *et al.* 2015; Amestoy *et al.* 2016; Wang *et al.* 2019; Kamath *et al.* 2021). This simplified physics implies that the solid Earth is viewed as a fluid, ignoring its elastic properties. Although elastic effects in many hydrophone dataset are weak, due to sources and receivers typically in the water, limited time window recording essentially *P*-wave phases and soft seabed generating weak *P*-to-*S* conversion, they can still be observed on the *P*-wave amplitudes [amplitude versus offset (AVO) effect], and therefore have a direct impact on acoustic FWI (Barnes & Charara 2009). To mitigate elastic effects, several methods have been developed, such as the use of Wiener filters and estimated V_p/V_s models to convert elastic data into pseudo-acoustic data in acoustic FWI (Agudo *et al.* 2018, 2020), or more recently the use of neural networks to obtain an acoustic version of the elastic data in the data processing (Yao *et al.* 2020). Those methods aim at improving the stability of *P*-wave velocity reconstruction in the (visco-)acoustic approximation, disregarding the *S*-wave velocity reconstruction, which significantly reduces the computational cost of FWI. However, reconstructing jointly *P*- and *S*-wave velocity models could significantly improve the subsurface characterization, especially for the indication of fluid content (Sears *et al.* 2008, 2010; Prieux *et al.* 2013b). To better simulate the wave propagation physics and make good use of the recorded elastic information from 3C geophones in the ocean-bottom acquisition, the FWI based on an elastic approximation for the subsurface may be worth the extra computational cost.

An accurate and efficient forward modelling is vital for the success of FWI. To simulate elastic effects in marine environments, modelling of seismic wave propagation would require to be implemented in fluid–solid coupled media. Typically, there are two approaches to model the seismic wave propagation in such settings: monolithic and partitioned approaches (Hou *et al.* 2012; De Basabe & Sen 2015). The monolithic approach uses the same governing equation in both fluid and solid domains, and the fluid–solid interface is tackled implicitly. Usually, this approach requires much more sampling nodes to reduce dispersion and discretization errors near the interface (De Basabe & Sen 2015). Moreover, the first-order elastic wave-equation based monolithic approach incurs additional computing and storing of the vector wavefields in the fluid domain (Sethi *et al.* 2021), and the second-order elastic wave-equation based monolithic approach yields strong artefacts in the fluid region when using a conventional spectral-element (SEM) method for the discretization (Komatitsch *et al.* 2000). Those shortcomings lead us to consider the partitioned approach for the simulations in fluid–solid coupled media. The medium is divided into solid and fluid domains, in which the acoustic wave equation is used to describe the wave propagation in the fluid domain, while the elastic wave equation models elastic vibrations in the solid domain. Explicit fluid–solid boundary conditions express the mutual interaction between these two domains. Consequently, the forward problem in the fluid–solid coupled medium is described by an acoustic–elastic coupled wave-equation system, and the corresponding methodology of FWI gradient building can be developed through the adjoint-state method (Plessix 2006). The elastic wave equation is based on the second-order partial differential equation of displacement vector for memory savings. Regarding the acoustic wave equation, it can be formulated in terms of different variables, such as pressure, velocity potential, displacement potential and displacement (Everstine 1997). Consequently, the acoustic–elastic coupled wave-equation system can be formulated in diverse ways (Feng 2000; Komatitsch *et al.* 2000; Chaljub & Valette 2004; Ross *et al.* 2009; Mönkölä 2011), allowing various possibilities for our FWI design.

In this study, we aim at developing a flexible and efficient 3D fluid–solid coupled FWI engine to achieve a high-resolution multiparameter reconstruction of the subsurface. We use a time-domain spectral-element method (SEM) with a 3-D Cartesian-based hexahedral mesh for implementing both forward and adjoint problems. The choice of SEM is motivated by its high accuracy in dealing with the boundary conditions through interface integral, conforming an irregular interface through flexible mesh deformations, and its high computational efficiency through domain-decomposition based parallelization (Komatitsch 1997; Peter *et al.* 2011; Trinh *et al.* 2019). In the following sections, we first review the procedure of formulating the fluid–solid coupled problem into an acoustic–elastic coupled wave-equation system (Cao *et al.* 2020a, b), which is followed by the definition of the associated FWI problem and the derivation of the FWI misfit function gradient expression for different parameters based on the adjoint-state method. A hybrid approach is proposed here for the gradient building, which makes it possible to re-exploit the explicit forward modelling solver for the solution of the adjoint system. Next, we illustrate the recipe of Cartesian-based SEM in the construction of an accurate and efficient acoustic–elastic coupled wave modelling solver which can be used in both forward and adjoint simulations. Then, we move to numerical studies of the proposed method. For the purpose of validation, several forward modelling benchmark tests are carried out, with the help of the semi-analytical solution package Gar6more2D (Diaz & Ezziani 2008) in 2-D and the open-source spectral-element package SPECFEM3D (Peter *et al.* 2011) in 3-D. The gradient kernels in the FWI part show how *P*- and *S*-wave velocity models can be inferred from data. From the aspect of application, two fluid–solid coupled FWI case studies on a 3-D extended Marmousi-II model and a 3-D deep-water crustal-scale model are performed. They illustrate how we can benefit from ocean-bottom seismic acquisition through the reconstruction of *S*-wave velocity models using 3C geophone data.

2 METHODOLOGY FOR FLUID–SOLID COUPLED FWI

In the fluid–solid coupled problem, there are various formulations existing for describing the interaction between acoustic and elastic waves. Here we consider 4 commonly used formulations for the acoustic–elastic coupled wave-equation system. For each of them, the displacement field is solved in the elastic wave equation, while the acoustic wave equation is formulated in terms of pressure, velocity potential, displacement potential and displacement, respectively.

2.1 Fluid–solid coupled forward problem

In the solid domain, the complete form of the elastic wave equation can be written as

$$\rho_s \partial_{tt}\mathbf{u}_s = \nabla\cdot\boldsymbol{\sigma} + \mathbf{f}_s, \qquad \boldsymbol{\sigma} = \mathbf{C}:\boldsymbol{\epsilon}, \qquad \boldsymbol{\epsilon} = \tfrac{1}{2}\left[\nabla\mathbf{u}_s + (\nabla\mathbf{u}_s)^T\right], \tag{1}$$

where $\mathbf{u}_s$ and $\mathbf{f}_s$ are the displacement and force vectors, respectively, $\boldsymbol{\sigma}$ is the second-order stress tensor, $\boldsymbol{\epsilon}$ is the second-order strain tensor, ρ_s is the solid density and $\mathbf{C}$ is the fourth-order elastic stiffness tensor.

In the fluid domain, the wavefield is governed by the following conservation and dynamic equations with an irrotational and inviscid assumption

$$\rho_f \partial_{tt}\mathbf{u}_f + \nabla P = \mathbf{f}_f, \qquad \partial_t P + \kappa\nabla\cdot\partial_t\mathbf{u}_f = 0, \tag{2}$$

where $\mathbf{u}_f$ and $\mathbf{f}_f$ are the displacement and force vectors in the fluid domain, respectively, P is the pressure, ρ_f is the fluid density, and κ is the bulk modulus of the fluid. By substitution and elimination, eq. (2) can be rewritten in terms of fluid pressure (P), displacement potential (φ), velocity potential (ϕ) or displacement ($\mathbf{u}_f$), respectively:

$$\begin{aligned}
&\partial_{tt}P + \kappa\nabla\cdot\left(-\frac{1}{\rho_f}\nabla P\right) = P_f,\\
&\partial_{tt}\varphi - \kappa\nabla\cdot\left(\frac{1}{\rho_f}\nabla\varphi\right) = \iint -P_f \mathrm{d}t\mathrm{d}t,\\
&\partial_{tt}\phi - \frac{\kappa}{\rho_f}\nabla\cdot\nabla\phi = \int -\frac{1}{\rho_f}P_f \mathrm{d}t,\\
&\partial_{tt}\mathbf{u}_f - \frac{1}{\rho_f}\nabla\left(\kappa\nabla\cdot\mathbf{u}_f\right) = \frac{1}{\rho_f}\mathbf{f}_f.
\end{aligned} \tag{3}$$

Here, P_f is the pressure source associated with the force vector $\mathbf{f}_f$ through

$$P_f = -\kappa\nabla\cdot\left(\frac{1}{\rho_f}\mathbf{f}_f\right), \tag{4}$$

and the velocity potential ϕ and displacement potential φ are defined by

$$\partial_t\mathbf{u}_f := \nabla\phi, \qquad \mathbf{u}_f := \frac{1}{\rho}\nabla\varphi. \tag{5}$$

Their relationships with the pressure P follow:

$$P = -\rho\partial_t\phi, \qquad P = -\partial_{tt}\varphi. \tag{6}$$

Accordingly, the boundary conditions at the fluid–solid interface (Γ_{fs}) can be expressed in 4 different ways, leading to the following formulations for representing the acoustic–elastic coupled wave-equation system:

(1)$P-\mathbf{u}_s$ formulation

$$\begin{aligned}
\tfrac{1}{\kappa}\partial_{tt}P - \nabla\cdot\left(\tfrac{1}{\rho_f}\nabla P\right) &= \tfrac{1}{\kappa}P_f, && \text{in } \Omega_f,\\
\rho_s\partial_{tt}\mathbf{u}_s = \nabla\cdot\boldsymbol{\sigma} + \mathbf{f}_s, \quad \boldsymbol{\sigma} &= \mathbf{C}:\boldsymbol{\epsilon}, && \text{in } \Omega_s,\\
\partial_{tt}\mathbf{u}_s\cdot\mathbf{n} = -\tfrac{1}{\rho_f}\nabla P\cdot\mathbf{n}, \quad \boldsymbol{\sigma}_s\cdot\mathbf{n} &= -P\mathbf{n}, && \text{on } \Gamma_{fs};
\end{aligned} \tag{7}$$

(2)$\varphi-\mathbf{u}_s$ formulation

$$\begin{aligned}
\frac{1}{\kappa}\partial_{tt}\varphi - \nabla\cdot\left(\frac{1}{\rho_f}\nabla\varphi\right) &= \frac{1}{\kappa}\iint -P_f\mathrm{d}t\mathrm{d}t, && \text{in } \Omega_f,\\
\rho_s\partial_{tt}\mathbf{u}_s = \nabla\cdot\boldsymbol{\sigma} + \mathbf{f}_s, \quad \boldsymbol{\sigma} &= \mathbf{C}:\boldsymbol{\epsilon}, && \text{in } \Omega_s,\\
\mathbf{u}_s\cdot\mathbf{n} = \frac{1}{\rho_f}\nabla\varphi\cdot\mathbf{n}, \quad \boldsymbol{\sigma}_s\cdot\mathbf{n} &= \partial_{tt}\varphi\mathbf{n}, && \text{on } \Gamma_{fs};
\end{aligned} \tag{8}$$

(3)$\phi-\mathbf{u}_s$ formulation

$$\begin{aligned}
\frac{1}{\kappa}\partial_{tt}\phi - \frac{1}{\rho_f}\nabla\cdot\nabla\phi &= \frac{1}{\kappa}\int -\frac{1}{\rho_f}P_f\mathrm{d}t, && \text{in } \Omega_f,\\
\rho_s\partial_{tt}\mathbf{u}_s = \nabla\cdot\boldsymbol{\sigma} + \mathbf{f}_s, \quad \boldsymbol{\sigma} &= \mathbf{C}:\boldsymbol{\epsilon}, && \text{in } \Omega_s,\\
\partial_t\mathbf{u}_s\cdot\mathbf{n} = \nabla\phi\cdot\mathbf{n}, \quad \boldsymbol{\sigma}_s\cdot\mathbf{n} &= \rho_f\partial_t\phi\mathbf{n}, && \text{on } \Gamma_{fs};
\end{aligned} \tag{9}$$

(4)$\mathbf{u}_f - \mathbf{u}_s$ formulation

$$\begin{aligned} \rho_f \partial_{tt}\mathbf{u}_f &= \nabla\left(\kappa\nabla\cdot\mathbf{u}_f\right) + \mathbf{f}_f, \quad \text{in } \Omega_f, \\ \rho_s \partial_{tt}\mathbf{u}_s &= \nabla\cdot\boldsymbol{\sigma} + \mathbf{f}_s, \quad \boldsymbol{\sigma} = \mathbf{C}:\boldsymbol{\epsilon}, \quad \text{in } \Omega_s, \\ \mathbf{u}_s\cdot\mathbf{n} = \mathbf{u}_f\cdot\mathbf{n}, &\quad \boldsymbol{\sigma}_s\cdot\mathbf{n} = \kappa\left(\nabla\cdot\mathbf{u}_f\right)\mathbf{n}, \quad \text{on } \Gamma_{fs}, \end{aligned} \tag{10}$$

where the domains Ω_f and Ω_s denote the fluid and solid regions, respectively, and the boundary Γ_{fs}, which can be any continuous curvilinear shape, denotes the fluid–solid interface with a unit normal vector $\mathbf{n}$. Note that the continuity of normal component of displacement ($\mathbf{u}\cdot\mathbf{n}$) in the fluid–solid boundary condition has been modified in $P-\mathbf{u}_s$ and $\phi-\mathbf{u}_s$ formulations, where only the normal component of acceleration $\partial_{tt}\mathbf{u}$ and velocity $\partial_t\mathbf{u}$ are enforced to be continuous, respectively. In addition, as shown above, only the $\mathbf{u}_f-\mathbf{u}_s$ formulation uses a vector-valued equation in the fluid domain, which incurs additional costs of computing and storing compared with the other three approaches using a scalar-valued equation. For the sake of computing efficiency, we thus focus on the $P-\mathbf{u}_s$, $\varphi-\mathbf{u}_s$ and $\phi-\mathbf{u}_s$ formulations, where a scalar-valued equation is considered in the fluid domain.

2.2 Fluid–solid coupled inversion problem

FWI on ocean-bottom seismic data can be formulated as the following minimization problem:

$$\min_{\mathbf{m}} J(\mathbf{m}), \quad \mathbf{m} = \left(\rho_f, \kappa; \rho_s, C_{ijkl}\right), \tag{11}$$

where the misfit function $J(\mathbf{m})$ is defined by

$$J(\mathbf{m}) = \tfrac{1}{2}\textstyle\sum_{s,r}\left(\alpha_s\|\mathbf{S}_{s,r}\mathbf{W}_P(\mathbf{m}) - \mathbf{d}_P^{\text{obs}}\|^2 + \beta_s\|\mathbf{S}_{s,r}\mathbf{W}_{\mathbf{u}}(\mathbf{m}) - \mathbf{d}_{\mathbf{u}}^{\text{obs}}\|^2\right). \tag{12}$$

Here the full wavefields of pressure $\mathbf{W}_P$ and displacement $\mathbf{W}_{\mathbf{u}}$ are extracted by the restriction operator $\mathbf{S}_{s,r}$ at the receiver position r for each source s to fit the corresponding observed pressure data $\mathbf{d}_P^{\text{obs}}$ and 3C displacement data $\mathbf{d}_{\mathbf{u}}^{\text{obs}}$, respectively. Due to a large order of magnitude difference between these two data, scaling factors α_s and β_s need to be introduced to render the two terms in the misfit function dimensionless when inverting them simultaneously. They can be determined by the L_2 norm of the observed data shot by shot, namely

$$\alpha_s = \frac{1}{\sum_r\|\mathbf{d}_P^{\text{obs}}\|^2}, \quad \beta_s = \frac{1}{\sum_r\|\mathbf{d}_{\mathbf{u}}^{\text{obs}}\|^2}. \tag{13}$$

The minimization of $J(\mathbf{m})$ is performed through local optimization techniques, more precisely a quasi-Newton l-BFGS method, which requires access to the gradient of $J(\mathbf{m})$ at each iteration (Nocedal 1980). Following the conventional FWI scheme, this minimization problem is subjected to the forward wave-equation constraint, namely the acoustic–elastic coupled wave-equation system formulated in terms of eqs (7), (8) or (9). The resulting gradient can be obtained from the zero-lag cross-correlation of forward wavefields and adjoint wavefields, through the adjoint-state method (Plessix 2006).

The adjoint wavefields in both fluid and solid domains come by solving the adjoint system of the acoustic–elastic coupled wave equations. Thanks to the Lagrange multiplier technique, a Lagrangian L is constructed by including both the misfit function $J(\mathbf{m})$ and the acoustic–elastic coupled wave-equation constraint, whose stationary points with respect to wavefield variables can generate the resulting adjoint system. As an example, a detailed mathematical derivation for the adjoint system of the $P-\mathbf{u}_s$ formulation is provided in the Appendix A, and adjoint systems of the other two formulations ($\varphi-\mathbf{u}_s$ and $\phi-\mathbf{u}_s$ formulations) can also be obtained in an analogous way. The expressions of those adjoint systems are summarized as follows:

(1)The adjoint system of the $P-\mathbf{u}_s$ formulation

$$\begin{aligned} \frac{1}{\kappa}\partial_{tt}\mu^{(P)} - \nabla\cdot\left(\frac{1}{\rho_f}\nabla\mu^{(P)}\right) &= \textstyle\sum_{s,r}\alpha_s\mathbf{S}_{s,r}^T\left(\mathbf{S}_{s,r}\mathbf{W}_P - \mathbf{d}_P^{\text{obs}}\right), \quad \text{in } \Omega_f, \\ \rho_s\partial_{tt}\boldsymbol{\lambda} = \nabla\cdot\mathbf{T} + \textstyle\sum_{s,r}\beta_s\mathbf{S}_{s,r}^T\left(\mathbf{S}_{s,r}\mathbf{W}_{\mathbf{u}} - \mathbf{d}_{\mathbf{u}}^{\text{obs}}\right), &\quad \mathbf{T} = \mathbf{C}:\nabla\boldsymbol{\lambda}, \quad \text{in } \Omega_s, \\ \boldsymbol{\lambda}\cdot\mathbf{n} = \frac{1}{\rho_f}\nabla\mu^{(P)}\cdot\mathbf{n}, &\quad \mathbf{T}\cdot\mathbf{n} = \partial_{tt}\mu^{(P)}\mathbf{n}, \quad \text{on } \Gamma_{fs}. \end{aligned} \tag{14}$$

(2)The adjoint system of the $\varphi-\mathbf{u}_s$ formulation

$$\begin{aligned} \frac{1}{\kappa}\partial_{tt}\mu^{(\varphi)} - \nabla\cdot\left(\frac{1}{\rho_f}\nabla\mu^{(\varphi)}\right) &= -\textstyle\sum_{s,r}\alpha_s\mathbf{S}_{s,r}^T\partial_{tt}\left(\mathbf{S}_{s,r}\mathbf{W}_P - \mathbf{d}_P^{\text{obs}}\right), \quad \text{in } \Omega_f, \\ \rho_s\partial_{tt}\boldsymbol{\lambda} = \nabla\cdot\mathbf{T} + \textstyle\sum_{s,r}\beta_s\mathbf{S}_{s,r}^T\left(\mathbf{S}_{s,r}\mathbf{W}_{\mathbf{u}} - \mathbf{d}_{\mathbf{u}}^{\text{obs}}\right), &\quad \mathbf{T} = \mathbf{C}:\nabla\boldsymbol{\lambda}, \quad \text{in } \Omega_s, \\ \partial_{tt}\boldsymbol{\lambda}\cdot\mathbf{n} = -\frac{1}{\rho_f}\nabla\mu^{(\varphi)}\cdot\mathbf{n}, &\quad \mathbf{T}\cdot\mathbf{n} = -\mu^{(\varphi)}\mathbf{n}, \quad \text{on } \Gamma_{fs}. \end{aligned} \tag{15}$$

(3)The adjoint system of the $\phi - \mathbf{u}_s$ formulation

$$\begin{aligned}
&\frac{1}{\kappa}\partial_{tt}\mu^{(\phi)} - \nabla\cdot\left(\frac{1}{\rho_f}\nabla\mu^{(\phi)}\right) = \frac{1}{\rho_f}\sum\nolimits_{s,r}\alpha_s\mathbf{S}_{s,r}^T\partial_t\left(\mathbf{S}_{s,r}\mathbf{W}_P - \mathbf{d}_P^{\text{obs}}\right), \quad \text{in } \Omega_f,\\
&\rho_s\partial_{tt}\boldsymbol{\lambda} = \nabla\cdot\mathbf{T} + \sum\nolimits_{s,r}\beta_s\mathbf{S}_{s,r}^T\left(\mathbf{S}_{s,r}\mathbf{W}_{\mathbf{u}} - \mathbf{d}_{\mathbf{u}}^{\text{obs}}\right), \quad \mathbf{T} = \mathbf{C}:\nabla\boldsymbol{\lambda}, \quad \text{in } \Omega_s,\\
&\partial_t\boldsymbol{\lambda}\cdot\mathbf{n} = \nabla\mu^{(\phi)}\cdot\mathbf{n}, \qquad \mathbf{T}\cdot\mathbf{n} = \rho_f\partial_t\mu^{(\phi)}\mathbf{n}, \quad \text{on } \Gamma_{fs},
\end{aligned} \tag{16}$$

where the adjoint wavefields $\mu^{(P)}$, $\mu^{(\varphi)}$ and $\mu^{(\phi)}$ are associated with pressure P, displacement potential φ and velocity potential ϕ in the fluid domain, respectively. In the solid domain, the vectorial adjoint wavefield $\boldsymbol{\lambda}$ is associated with the displacement vector $\mathbf{u}$. Their corresponding gradient expressions of density ρ and bulk modulus κ in the fluid domain can be written as

$$\frac{\partial J(\mathbf{m})}{\partial\rho} = \left(\nabla\mu^{(P)}, \tfrac{1}{\rho_f^2}\nabla P\right)_{\Omega_f,t} \quad \text{and} \quad \frac{\partial J(\mathbf{m})}{\partial\kappa} = \left(\mu^{(P)}, \tfrac{1}{\kappa^2}\partial_{tt}P\right)_{\Omega_f,t}, \tag{17}$$

$$\frac{\partial J(\mathbf{m})}{\partial\rho} = \left(\nabla\mu^{(\varphi)}, \tfrac{1}{\rho_f^2}\nabla\varphi\right)_{\Omega_f,t} \quad \text{and} \quad \frac{\partial J(\mathbf{m})}{\partial\kappa} = \left(\mu^{(\varphi)}, \tfrac{1}{\kappa^2}\partial_{tt}\varphi\right)_{\Omega_f,t}, \tag{18}$$

$$\frac{\partial J(\mathbf{m})}{\partial\rho} = \left(\nabla\mu^{(\phi)}, \nabla\phi\right)_{\Omega_f,t} \quad \text{and} \quad \frac{\partial J(\mathbf{m})}{\partial\kappa} = \left(\mu^{(\phi)}, \tfrac{\rho_f^2}{\kappa^2}\partial_{tt}\phi\right)_{\Omega_f,t}. \tag{19}$$

For the solid domain, however, each fluid–solid coupled formulation shares the same gradient expressions due to a unique formulation used for the elastic wave equation, where the gradient expressions of density ρ and elastic stiffness tensor $\mathbf{C}$ are given by

$$\frac{\partial J(\mathbf{m})}{\partial\rho} = -\left(\boldsymbol{\lambda}, \partial_{tt}\mathbf{u}\right)_{\Omega_s,t} \quad \text{and} \quad \frac{\partial J(\mathbf{m})}{\partial C_{ijkl}} = -\left(\nabla\boldsymbol{\lambda}, \tfrac{\partial\mathbf{C}}{\partial C_{ijkl}} :: \nabla\mathbf{u}\right)_{\Omega_s,t}. \tag{20}$$

Consequently, we get three ways to construct the gradient kernels in the fluid–solid coupled FWI in terms of $P - \mathbf{u}_s$ formulation, $\varphi - \mathbf{u}_s$ formulation and $\phi - \mathbf{u}_s$ formulation, respectively. Note that among three adjoint systems, only the $\phi - \mathbf{u}_s$ formulation is self-adjoint, namely the forward and associated adjoint systems share the same structure. Systems based on the other two formulations are not self-adjoint. The self-adjoint property of the $\phi - \mathbf{u}_s$ formulation makes it attractive to re-exploit the forward modelling solver for getting the solution of the adjoint system. However, the time discretization in the next section will show that the $\phi - \mathbf{u}_s$ formulation is implicit in time and usually needs to involve a large matrix inverse during the solution, while the $P - \mathbf{u}_s$ and $\varphi - \mathbf{u}_s$ formulations are explicit in time and can be solved by an efficient time-marching scheme. In addition, we find an interesting property that the adjoint system of the $P - \mathbf{u}_s$ formulation shares the same structure as the forward system of the $\varphi - \mathbf{u}_s$ formulation, and reciprocally, the adjoint system of the $\varphi - \mathbf{u}_s$ formulation shares the same structure as the forward system of the $P - \mathbf{u}_s$ formulation.

Inspired by this reciprocity, we consider to design a new approach for the gradient building in the fluid–solid coupled FWI, which not only avoids the use of an implicit time scheme, but also keeps the feature of using the same modelling solver in the solution of both forward and adjoint problems. To achieve this goal, there are two options based on the gradient expressions (17) and (18). The forward and adjoint wavefields required in each expression can be computed with the same explicit modelling solver based on a hybrid combination of the $P - \mathbf{u}_s$ and $\varphi - \mathbf{u}_s$ formulations. However, the adjoint wavefield $\mu^{(\varphi)}$ in the gradient expression (18) relies on the solution of adjoint system (15), whose adjoint source involves a double time-derivative of the data residual that could magnify the high-frequency data-misfit noise on the receiver side (It will be demonstrated in the numerical validation section). Therefore, we choose an implementation based on the gradient expression 17. To calculate this gradient expression, we first extract the pressure wavefield P from the $\varphi - \mathbf{u}_s$ based forward modelling, and then get the adjoint wavefield $\mu^{(P)}$ by solving the $P - \mathbf{u}_s$ adjoint system which has the same structure as the $\varphi - \mathbf{u}_s$ forward system as noted before. Doing so, we can benefit from (1) exploiting the same modelling solver for both adjoint and forward modelling, (2) using explicit time stepping algorithms and (3) avoiding involving double time-derivatives in the source term of the adjoint system. A detailed algorithm workflow of this hybrid approach is summarized as follows:

Step 1: Solve the $\varphi - \mathbf{u}_s$ forward system (eq. 8) for the forward wavefields φ in the fluid domain and $\mathbf{u}_s$ in the solid domain.

Step 2: Extract the pressure wavefield P from the forward wavefield φ obtained in Step 1 by $P = -\partial_{tt}\varphi$ (eq. 6).

Step 3: Based on the deduced pressure wavefield in Step 2, solve the adjoint $P - \mathbf{u}_s$ system (eq. 14) with the same explicit modelling solver as in Step 1 for the adjoint wavefields $\mu^{(P)}$ in the fluid domain and $\boldsymbol{\lambda}$ in the solid domain.

Step 4: Compute the zero-lag cross-correlation of the forward and the adjoint wavefields to get the elementary gradients with the help of pressure forward and adjoint wavefields (eq. 17) and the help of displacement forward and adjoint wavefields (eq. 20). The gradient for some other parameters, such as P-wave (V_p) and S-wave (V_s) velocities, can be calculated by the chain rule based on them.

3 SEM-BASED IMPLEMENTATION

Theoretically, the three acoustic–elastic coupled formulations mentioned above can all be used for modelling the wave propagation in the fluid–solid coupled media. However, from the aspect of numerical implementation, each of them has its own pros and cons.

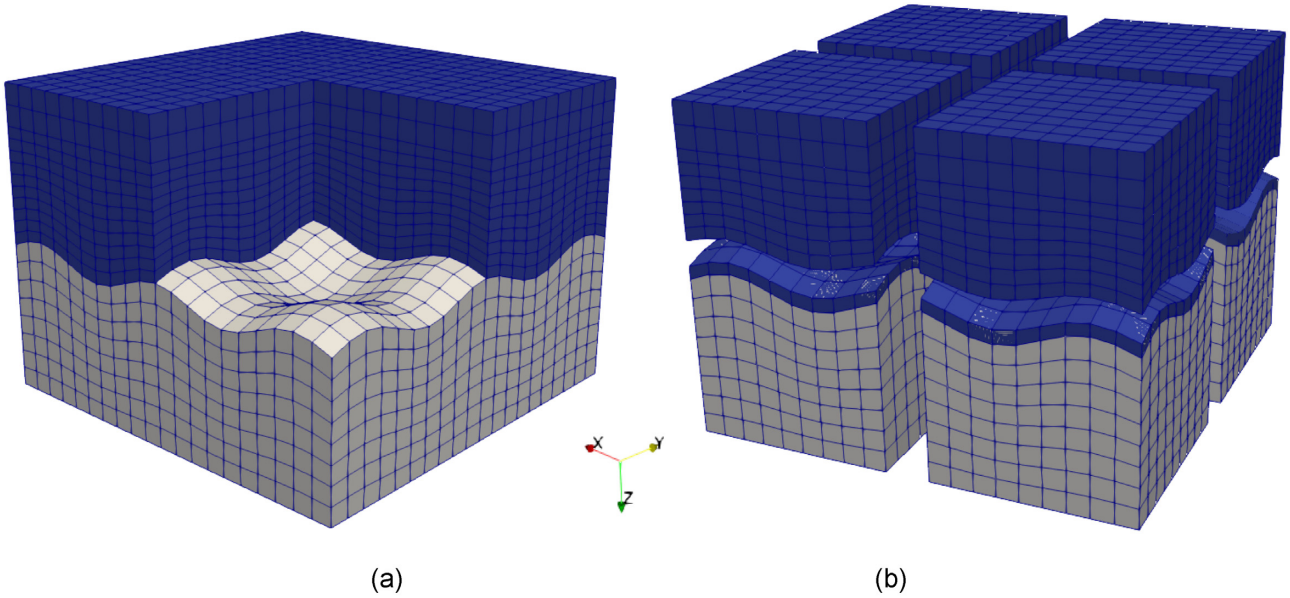

Figure 1. Cartesian-based hexahedral mesh in the SEM discretization (a) and 8 partitions on parallel cores (b). Here the blue parts indicate the fluid domain.

3.1 Generalities

Up to now, a wide range of numerical discretization methods has been developed for solving the acoustic and elastic partial differential equations (PDE). Among them, the finite-difference (FD) method is commonly used due to its numerical efficiency and relatively simple implementation (Kelly *et al.* 1976; Virieux 1986). However, the standard FD method has some numerical difficulties in the correct implementation of the boundary conditions at specific interfaces, such as the fluid–solid interface, and an extra effort and trade-off of accuracy and complexity are always required (De Basabe & Sen 2015; Sun *et al.* 2017; Sethi *et al.* 2021). As an alternative, here we adopt the spectral-element method (SEM) for the spatial discretization, which is a specific finite-element method based on the weak form of the PDE. This method has the geometric flexibility of the finite-element method and the high accuracy of a spectral convergence. In SEM, the wavefield discretization is accomplished by using high-order Lagrange interpolants on hexahedral elements, and the integration over elements are based on the Gauss–Lobatto–Legendre (GLL) points so as to yield a diagonal mass matrix (Komatitsch 1997; Komatitsch & Vilotte 1998; Komatitsch & Tromp 1999). Compared with standard finite-element methods, such a diagonal mass matrix avoids the mass matrix inversion in explicit-time marching schemes, making it easily parallel and efficient in the large-scale problem computation. More importantly, the weak form in SEM ensures that the fluid–solid boundary conditions can be easily and accurately implemented in both fluid and solid domains through a surface integral over the interface. As an example, we give the weak form of the $P-\mathbf{u}_s$ formulation (eq. 7) as follows:

$$\begin{aligned}
&\int_{\Omega_f}\frac{1}{\kappa}\partial_{tt}P w\mathrm{d}\Omega+\int_{\Omega_f}\frac{1}{\rho_f}\nabla w\cdot\nabla P\mathrm{d}\Omega-\int_{\Gamma_{fs}}w\partial_{\mathbf{tt}}\mathbf{u}_s\cdot\mathbf{n}\mathrm{d}\Gamma=\int_{\Omega_f}\frac{1}{\kappa}P_f w\mathrm{d}\Omega,\\
&\int_{\Omega_s}\rho_s\partial_{\mathbf{tt}}\mathbf{u}_s\cdot\mathbf{w}\mathrm{d}\Omega+\int_{\Omega_s}\nabla\mathbf{w}:\boldsymbol{\sigma}\mathrm{d}\Omega+\int_{\Gamma_{fs}}\mathbf{w}\cdot P\mathbf{n}\mathrm{d}\Gamma=\int_{\Omega_s}\mathbf{f}_s\cdot\mathbf{w}\mathrm{d}\Omega,
\end{aligned}\tag{21}$$

where scalar w and vector $\mathbf{w}$ are the test functions in the fluid and solid domains, respectively, and the fluid–solid boundary conditions are naturally embedded within the third term on the left hand side by means of surface integrals.

3.2 Cartesian-based hexahedral mesh

In the SEM implementation, we consider using a Cartesian-based hexahedral mesh, which allows for conforming complex surface geometry through a high-order polynomial based vertical deformation of elements (Fig. 1a). Owing to its easy implementation and accurate surface conforming, this kind of structured mesh has been widely used in simulations of wave problems, such as the hyperbolic PDEs simulation engine ExaHyPE (Reinarz *et al.* 2020) which uses the discontinuous Galerkin (DG) method, the curvilinear and mimetic finite-difference methods in handling surface topography (Hestholm & Ruud 1998, 2002; Tarrass *et al.* 2011; Zhang *et al.* 2012; de la Puente *et al.* 2014; Konuk & Shragge 2019). Compared with general unstructured meshes as the one used in SPECFEM (Peter *et al.* 2011), this Cartesian-based mesh requires the number of elements in x-, y- and z-directions to be constant in both fluid and solid domains (although the size of elements can vary, see Fig. 1a), which makes it less practical in the application of local mesh refinement and tilting seabed scenarios where the size of elements in the shallow-water area need to be compressed. However, from the aspect of parallel computing, this mesh is convenient for partitioning in the domain decomposition as shown in Fig. 1(b). In this partition, we do not rely on an additional external partitioner, such as SCOTCH (Pellegrini 2018) or METIS (Karypis 2013), and the spatial position of each element is directly associated with three

element-indices like the conventional finite-difference implementation. In particular, elements in fluid and solid domains can be localized according to the element index in the vertical direction, without labelling the acoustic or elastic properties for each elements during the SEM modelling.

3.3 Time discretization: explicit or implicit scheme

After the spatial discretization in terms of spectral elements, we can get the semi-discretized systems associated with the weak forms of three acoustic–elastic coupled formulations. The matrix form of those semi-discretized systems are given by

$P - \mathbf{u}_s$ system

$$\begin{pmatrix} M_f & \mathbf{A} \\ \mathbf{0} & \mathbf{M}_s \end{pmatrix} \begin{pmatrix} \partial_{tt} P \\ \partial_{tt} \mathbf{u}_s \end{pmatrix} + \begin{pmatrix} D_f & \mathbf{0} \\ \mathbf{0} & \mathbf{D}_s \end{pmatrix} \begin{pmatrix} \partial_t P \\ \partial_t \mathbf{u}_s \end{pmatrix} + \begin{pmatrix} K_f & \mathbf{0} \\ \mathbf{A}^{\mathbf{T}} & \mathbf{K}_s \end{pmatrix} \begin{pmatrix} P \\ \mathbf{u}_s \end{pmatrix} = \begin{pmatrix} P_f \\ \mathbf{f}_s \end{pmatrix}, \tag{22}$$

$\varphi - \mathbf{u}_s$ system

$$\begin{pmatrix} M_f & \mathbf{0} \\ \mathbf{A}^{\mathbf{T}} & \mathbf{M}_s \end{pmatrix} \begin{pmatrix} \partial_{tt} \varphi \\ \partial_{tt} \mathbf{u}_s \end{pmatrix} + \begin{pmatrix} D_f & \mathbf{0} \\ \mathbf{0} & \mathbf{D}_s \end{pmatrix} \begin{pmatrix} \partial_t \varphi \\ \partial_t \mathbf{u}_s \end{pmatrix} + \begin{pmatrix} K_f & \mathbf{A} \\ \mathbf{0} & \mathbf{K}_s \end{pmatrix} \begin{pmatrix} \varphi \\ \mathbf{u}_s \end{pmatrix} = \begin{pmatrix} \varphi_f \\ \mathbf{f}_s \end{pmatrix}, \tag{23}$$

$\phi - \mathbf{u}_s$ system

$$\begin{pmatrix} M_f & \mathbf{0} \\ \mathbf{0} & \mathbf{M}_s \end{pmatrix} \begin{pmatrix} \partial_{tt} \phi \\ \partial_{tt} \mathbf{u}_s \end{pmatrix} + \begin{pmatrix} D_f & \mathbf{A} \\ \mathbf{A}^{\mathbf{T}} & \mathbf{D}_s \end{pmatrix} \begin{pmatrix} \partial_t \phi \\ \partial_t \mathbf{u}_s \end{pmatrix} + \begin{pmatrix} K_f & \mathbf{0} \\ \mathbf{0} & \mathbf{K}_s \end{pmatrix} \begin{pmatrix} \phi \\ \mathbf{u}_s \end{pmatrix} = \begin{pmatrix} \phi_f \\ \mathbf{f}_s \end{pmatrix}, \tag{24}$$

where $\mathbf{A}$ is the coupling matrix obtained by the integral along the fluid–solid interface, and the remaining matrices correspond to conventional notations in SEM, namely, M_f and $\mathbf{M}_s$ are the mass matrices, D_f and $\mathbf{D}_s$ are the matrices for implementing absorbing boundary condition and K_d and $\mathbf{K}_s$ are the stiffness matrices.

For the time discretization, we use the finite difference to approximate time derivatives in the above semi-discretized systems. Let us illustrate that the $P - \mathbf{u}_s$ and $\varphi - \mathbf{u}_s$ systems lead to an explicit time-marching scheme, while the $\phi - \mathbf{u}_s$ system is implicit in time and needs to solve equations governing the fluid and solid domain simultaneously. We consider using the standard second-order central finite difference scheme to approximate the following time derivatives

$$\partial_{tt} P \approx \frac{P^{n+1} - 2P^n + P^{n-1}}{\triangle t^2}, \quad \partial_t P \approx \frac{P^{n+1} - P^{n-1}}{2\triangle t}, \tag{25}$$

where P can be replaced by other wavefields like φ, ϕ and $\mathbf{u}_s$. The resulting discretized system of $\varphi - \mathbf{u}_s$ formulation is given by

$$M_f \frac{\varphi^{n+1} - 2\varphi^n + \varphi^{n-1}}{\triangle t^2} + D_f \frac{\varphi^{n+1} - \varphi^{n-1}}{2\triangle t} + K_f \varphi^n + \mathbf{A}\mathbf{u}_s^n = \varphi_f^n, \tag{26}$$

$$\mathbf{M}_s \frac{\mathbf{u}_s^{n+1} - 2\mathbf{u}_s^n + \mathbf{u}_s^{n-1}}{\triangle t^2} + \mathbf{D}_s \frac{\mathbf{u}_s^{n+1} - \mathbf{u}_s^{n-1}}{2\triangle t} + \mathbf{K}_s \mathbf{u}_s^n + \mathbf{A}^{\mathbf{T}} \frac{\varphi^{n+1} - 2\varphi^n + \varphi^{n-1}}{\triangle t^2} = \mathbf{f}_s^n. \tag{27}$$

It is easy to find that the time stepping is carried out explicitly. At each time step n, we first compute the displacement potential φ^{n+1} according to eq. (26) and then the displacement vector $\mathbf{u}^{n+1}$ from eq. (27). This time-marching procedure is also suitable for the $P - \mathbf{u}_s$ discretized system. By contrast, the time scheme for the $\phi - \mathbf{u}_s$ system is implicit as shown below:

$$M_f \frac{\phi^{n+1} - 2\phi^n + \phi^{n-1}}{\triangle t^2} + D_f \frac{\phi^{n+1} - \phi^{n-1}}{2\triangle t} + K_f \phi^n + \mathbf{A} \frac{\mathbf{u}_s^{n+1} - \mathbf{u}_s^{n-1}}{2\triangle t} = \phi_f^n, \tag{28}$$

$$\mathbf{M}_s \frac{\mathbf{u}_s^{n+1} - 2\mathbf{u}_s^n + \mathbf{u}_s^{n-1}}{\triangle t^2} + \mathbf{D}_s \frac{\mathbf{u}_s^{n+1} - \mathbf{u}_s^{n-1}}{2\triangle t} + \mathbf{K}_s \mathbf{u}_s^n + \mathbf{A}^{\mathbf{T}} \frac{\varphi^{n+1} - \varphi^{n-1}}{2\triangle t} = \mathbf{f}_s^n, \tag{29}$$

where ϕ^{n+1} and $\mathbf{u}^{n+1}$ need to be solved simultaneously, thus involving the inverse of the matrix

$$\begin{pmatrix} \frac{M_f}{\triangle t^2} + \frac{D_f}{2\triangle t} & \frac{\mathbf{A}}{2\triangle t} \\ \frac{\mathbf{A}^{\mathbf{T}}}{2\triangle t} & \frac{\mathbf{M}_s}{\triangle t^2} + \frac{\mathbf{D}_s}{2\triangle t} \end{pmatrix} \tag{30}$$

at each time step.

In our numerical implementation, the explicit finite-difference time-marching schemes for both $P - \mathbf{u}_s$ and $\varphi - \mathbf{u}_s$ discretized systems are achieved on the basis of Newmark scheme, written in a prediction-correction format (Komatitsch 1997). The corresponding algorithm for the $\varphi - \mathbf{u}_s$ system is summarized in Table 1 as an example. For the implicit scheme of the $\phi - \mathbf{u}_s$ discretized system, we still want to consider it in our following numerical comparison. Since a direct inverse of coefficient matrix is not affordable for large scale problem, we use an iterative Newmark scheme (Antonietti *et al.* 2020) listed in Table 2 as an alternative, which is based on a staggered prediction-multicorrection technique (Park & Felippa 1980) for the velocity correction.

Table 1. Newmark scheme for the $\varphi - \mathbf{u}_s$ system.

	Newmark scheme
1	Given initial conditions $\mathbf{u}^0$, $\partial_t \mathbf{u}^0$, $\partial_{tt} \mathbf{u}^0$, φ^0, $\partial_t \varphi^0$, $\partial_{tt} \varphi^0$
2	$\varphi^{n+1} = \varphi^n + \Delta t \partial_t \varphi^n + \frac{\Delta t^2}{2} \partial_{tt} \varphi^n$
3	$\mathbf{u}^{n+1} = \mathbf{u}^n + \Delta t \partial_t \mathbf{u}^n + \frac{\Delta t^2}{2} \partial_{tt} \mathbf{u}^n$
4	$\tilde{\varphi} = \partial_t \varphi^n + \frac{\Delta t}{2} \partial_{tt} \varphi^n$
5	$\tilde{\mathbf{u}} = \partial_t \mathbf{u}^n + \frac{\Delta t}{2} \partial_{tt} \mathbf{u}^n$
6	$\partial_{tt} \varphi^{n+1} = M^{-1} \left(F_{\text{ext}}^{n+1} - F_{\text{int}}^{n+1} \left(\varphi^{n+1}, \tilde{\varphi}, \mathbf{u}^{n+1} \right) \right)$
7	$\partial_{tt} \mathbf{u}^{n+1} = \mathbf{M}^{-1} \left(\mathbf{F}_{\text{ext}}^{n+1} - \mathbf{F}_{\text{int}}^{n+1} \left(\mathbf{u}^{n+1}, \tilde{\mathbf{u}}, \partial_{tt} \varphi^{n+1} \right) \right)$
8	$\partial_t \varphi^{n+1} = \tilde{\varphi} + \frac{\Delta t}{2} \partial_{tt} \varphi^{n+1}$
9	$\partial_t \mathbf{u}^{n+1} = \tilde{\mathbf{u}} + \frac{\Delta t}{2} \partial_{tt} \mathbf{u}^{n+1}$

Table 2. Staggered prediction/multicorrection Newmark scheme for the $\phi - \mathbf{u}_s$ system.

	Predictor-corrector staggered Newmark scheme
1	Given initial conditions $\mathbf{u}^0$, $\partial_t \mathbf{u}^0$, ϕ^0, $\partial_t \phi^0$
2	$\partial_{tt} \phi^n = M^{-1} \left(F_{\text{ext}}^n - F_{\text{int}}^n \left(\phi^n, \partial_t \phi^n, \partial_t \mathbf{u}^n \right) \right)$
3	$\partial_{tt} \mathbf{u}^n = \mathbf{M}^{-1} \left(\mathbf{F}_{\text{ext}}^n - \mathbf{F}_{\text{int}}^n \left(\mathbf{u}^n, \partial_t \mathbf{u}^n, \partial_t \phi^n \right) \right)$
4	$\phi^{n+1} = \phi^n + \Delta t \partial_t \phi^n + \frac{\Delta t^2}{2} \partial_{tt} \phi^n$
5	$\mathbf{u}^{n+1} = \mathbf{u}^n + \Delta t \partial_t \mathbf{u}^n + \frac{\Delta t^2}{2} \partial_{tt} \mathbf{u}^n$
6	$\tilde{\phi} = \partial_t \phi^n + \frac{\Delta t}{2} \partial_{tt} \phi^n$, $\partial_t \phi^{n+1} = \tilde{\phi}$
7	$\tilde{\mathbf{u}} = \partial_t \mathbf{u}^n + \frac{\Delta t}{2} \partial_{tt} \mathbf{u}^n$, $\partial_t \mathbf{u}^{n+1} = \tilde{\mathbf{u}}$
8	do $i = 1$, *niter*
9	$\partial_{tt} \phi^{n+1} = M^{-1} \left(F_{\text{ext}}^{n+1} - F_{\text{int}}^{n+1} \left(\phi^{n+1}, \tilde{\phi}, \partial_t \mathbf{u}^{n+1} \right) \right)$
10	$\partial_{tt} \mathbf{u}^{n+1} = \mathbf{M}^{-1} \left(\mathbf{F}_{\text{ext}}^{n+1} - \mathbf{F}_{\text{int}}^{n+1} \left(\mathbf{u}^{n+1}, \tilde{\mathbf{u}}, \partial_t \phi^{n+1} \right) \right)$
11	$\partial_t \phi^{n+1} = \tilde{\phi} + \frac{\Delta t}{2} \partial_{tt} \phi^{n+1}$
12	$\partial_t \mathbf{u}^{n+1} = \tilde{\mathbf{u}} + \frac{\Delta t}{2} \partial_{tt} \mathbf{u}^{n+1}$
13	end do

4 NUMERICAL VALIDATION

For the purpose of validation, we conduct various numerical tests from the forward modelling to the FWI gradient building. We compare pros and cons of the three acoustic–elastic coupled formulations in terms of accuracy and computational efficiency. The feasibility of the hybrid approach is illustrated in the gradient building. A load-balanced strategy is also introduced in the domain decomposition to enhance the performance of parallel computing.

4.1 Validation studies in 2-D space

We conduct the first validation study in a 2-D space for evaluating the numerical performance in both forward modelling and gradient building, which serves as the foundation for the design of an accurate and efficient 3-D fluid–solid coupled FWI engine.

4.1.1 Forward modelling

The SEM-based simulation accuracy of three coupled formulations ($P - \mathbf{u}_s$, $\phi - \mathbf{u}_s$ and $\varphi - \mathbf{u}_s$ formulations) is illustrated through the comparison with semi-analytical solutions in a 2-D bi-layered benchmark model (Diaz & Ezziani 2008). This model has a size of 31.2 km $\times$ 12 km and its physical parameters are listed in Table 3. The upper half-part is acoustic, while the lower half-part is elastic isotropic. An explosive pressure-source with a 10 Hz Ricker wavelet characteristic is applied 0.5 km above their interface. Thus, the minimum wavelength we consider in the modelling is $\lambda_{\min} = 1500/20 = 75$ m. In the SEM implementation, the 5th-order Lagrange polynomials are chosen as basis functions. By following its dispersion criteria of $h \leq \lambda_{\min}/1.2$ (Komatitsch 1997), the element size is set to be 60 m, and therefore the total number of elements for the model discretization is $520 \times 200 = 104\,000$. A time step of $\Delta t = 1$ ms is used in the test, which well satisfies the CFL condition $\Delta t \leq 0.3 \times 0.1175 \times \min(h/V_{\max})$. To match the semi-analytical solution, unlike the real marine environment, there is no free-surface boundary conditions at the top of the fluid layer, and all outgoing wavefields at the model boundaries are absorbed by a combination of the radiative boundary condition (Lysmer & Kuhlemeyer 1969) and sponge layers (Cerjan *et al.* 1985). For the three coupled

Table 3. Physical parameters of the bi-layered model used for the modelling solver test.

Media	Property ρ (kg m^{-3})	V_p (m s^{-1})	V_s (m s^{-1})	Anisotropy/Attenuation Parameters
Fluid	Acoustic	1000	1500	0
Solid	E-ISO	2500	3400	1963	N/A
	E-VTI				$\epsilon = 0.1, \delta = 0.4, \gamma = 0.2$
	E-TTI				$\epsilon = 0.1, \delta = 0.4, \gamma = 0.2$ $\theta = 45^\circ, \phi = 15^\circ$
	E-VISCO				$Q_p = 40, Q_s = 30$

formulations, the exponential tapering factors in sponge layers are directly applied onto the wavefield variables P, ϕ or φ in the fluid domain and $\mathbf{u}_s$ in the solid domain.

Fig. 2(a) shows an excellent agreement between all three numerical modelling results and the semi-analytical solution obtained from Gar6more2D (Diaz & Ezziani 2008) in terms of pressure and two displacement components, which are recorded on the seabed with an offset of 12.6 km. A further accuracy estimation, the continuity checking at the fluid–solid interface, is shown in Fig. 2(b), where we extract the normal displacements u_z at the interface from both fluid and solid sides and zoom-in the results from 7 to 10 s for clarifying the difference. From Fig. 2(b), we find that only the result using the $\varphi - \mathbf{u}_s$ formulation produces the same vertical displacement component from both fluid and solid sides. This is due to the fact that, instead of the normal displacement continuity, the other two formulations enforce the normal component of acceleration and velocity to be continuous, respectively. Thus, from the aspect of accuracy, $\varphi - \mathbf{u}_s$ formulation is a better choice for the fluid–solid coupled modelling.

However, when we look at the right-hand side (RHS) term of $\varphi - \mathbf{u}_s$ formulation in the fluid domain (eq. 8), a double time-integration of the source wavelet is required. According to the spectrum analysis in Fig. 3(a), this double time-integration pushes the peak frequency of $\varphi - \mathbf{u}_s$ formulation's RHS term towards the low frequency direction, and a similar phenomenon can also be observed on the RHS term of $\phi - \mathbf{u}_s$ formulation, due to its single time-integration of the source wavelet (eq. 9). Fig. 3(b) displays that those low-frequency components are harmful to the effectiveness of sponge layers in the absorption of fluid-related wavefield variables ϕ and φ (their energies in terms of L_2 norm decay slowly). However, the physical variable of interest in the fluid domain is pressure. According to eq. (6), it can be obtained through first- or second-order time-derivative of potential variables, and then we observe a similar absorption effectiveness for the pressure P even if using the different formulations (Fig. 3c). Analogously, an absorption comparison of displacement vector in the solid domain is illustrated in Fig. 3(d). In contrast to different wavefield variables in the fluid domain, the elastic wave equation in the solid is only formulated with the displacement vector, and therefore an identical absorption effectiveness is achieved for all three coupled formulations.

In addition, the comparison in terms of elapsed time and memory consumption in Table 4 reveals a higher computational efficiency of $P - \mathbf{u}_s$ and $\varphi - \mathbf{u}_s$ formulations, which benefits from their explicit time-marching schemes. By contrast, the staggered prediction-multicorrection iterative scheme for the $\phi - \mathbf{u}_s$ formulation is more expensive from a computational time point of view, which requires at least two iterations at each time step. Consequently, by a comprehensive consideration of the above continuity checking, absorbing effectiveness evaluation and computational cost, we conclude that the $\varphi - \mathbf{u}_s$ formulation achieves the best trade-off in terms of both efficiency and accuracy.

4.1.2 Gradient building

The conventional FWI gradient is a sum of gradient kernels associated with different source-receiver couples. Here we investigate the gradient kernels of a specific source–receiver couple in different computing approaches on a simple bi-layered model. We add perturbations of $+500$ m s^{-1} on the P-wave velocity, $+200$ m s^{-1} on the S-wave velocity and $+50$ kg m^{-3} on the density for the solid domain. The resulting gradient kernels of P-wave velocity, S-wave velocity and density are illustrated in Fig. 4. We see that the model parameters can be inferred from data through the contribution of different waves, such as the diving wave, reflected wave and P-to-S converted wave that supports the S-wave velocity reconstruction. It can be seen that the gradient kernels obtained from the hybrid approach are nearly identical with the other three gradient kernels following the $P - \mathbf{u}_s$, $\varphi - \mathbf{u}_s$ and $\phi - \mathbf{u}_s$ formulations rigorously, confirming the feasibility of the hybrid approach in the gradient building. A detailed comparison shows some high-frequency noise on the receiver side in the gradient kernels obtained from the $\varphi - \mathbf{u}_s$ formulation (the zones delineated by red squares in Fig. 4b). It is because a double time-derivative of the data residual is used as the adjoint source in the adjoint system of $\varphi - \mathbf{u}_s$ formulation (eq. 15), which magnifies the numerical oscillation in the data residual during the adjoint simulation. By contrast, the adjoint source used in the hybrid approach comes from the adjoint system of the $P - \mathbf{u}_s$ formulation (eq. 14), which is the data residual itself. Therefore, we select this hybrid approach for the gradient building in the following 3-D fluid–solid coupled FWI engine design.

4.2 3-D implementation and load balancing

We move to the design of 3-D SEM-based fluid–solid coupled FWI engine, in which a domain-decomposition parallelization strategy is used for improving the computational efficiency in large-scale problems. This 3-D implementation is embedded into the SEM46 code (SEM for

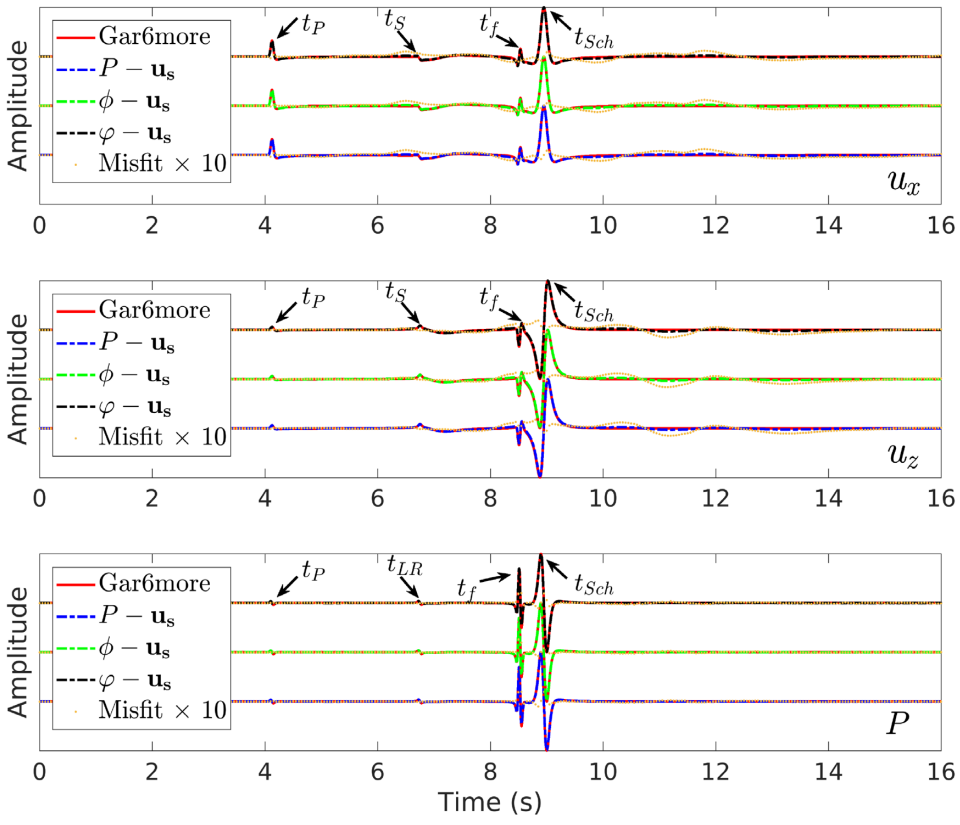

(a)

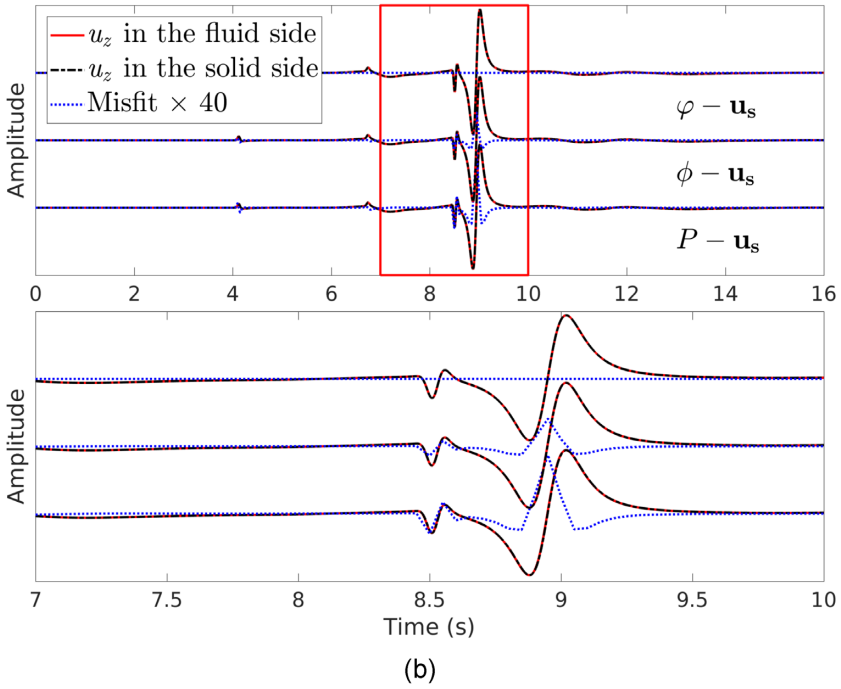

(b)

Figure 2. Validation of the modelling results in 2-D isotropic bi-layered model. (a) Benchmark against the semi-analytical solution (Gar6more2D (Diaz & Ezziani 2008)), (b) continuity checking at the fluid–solid interface. Receiver is located at the interface with an offset of 12.6 km. Here t_P, t_S/t_{LR}, t_f, t_{Sch} denote the arrival time of *P*-wave, *S*-wave (solid)/leak Rayleigh wave (fluid), fluid acoustic wave and Scholte wave, respectively (Zhu *et al.* 2004).

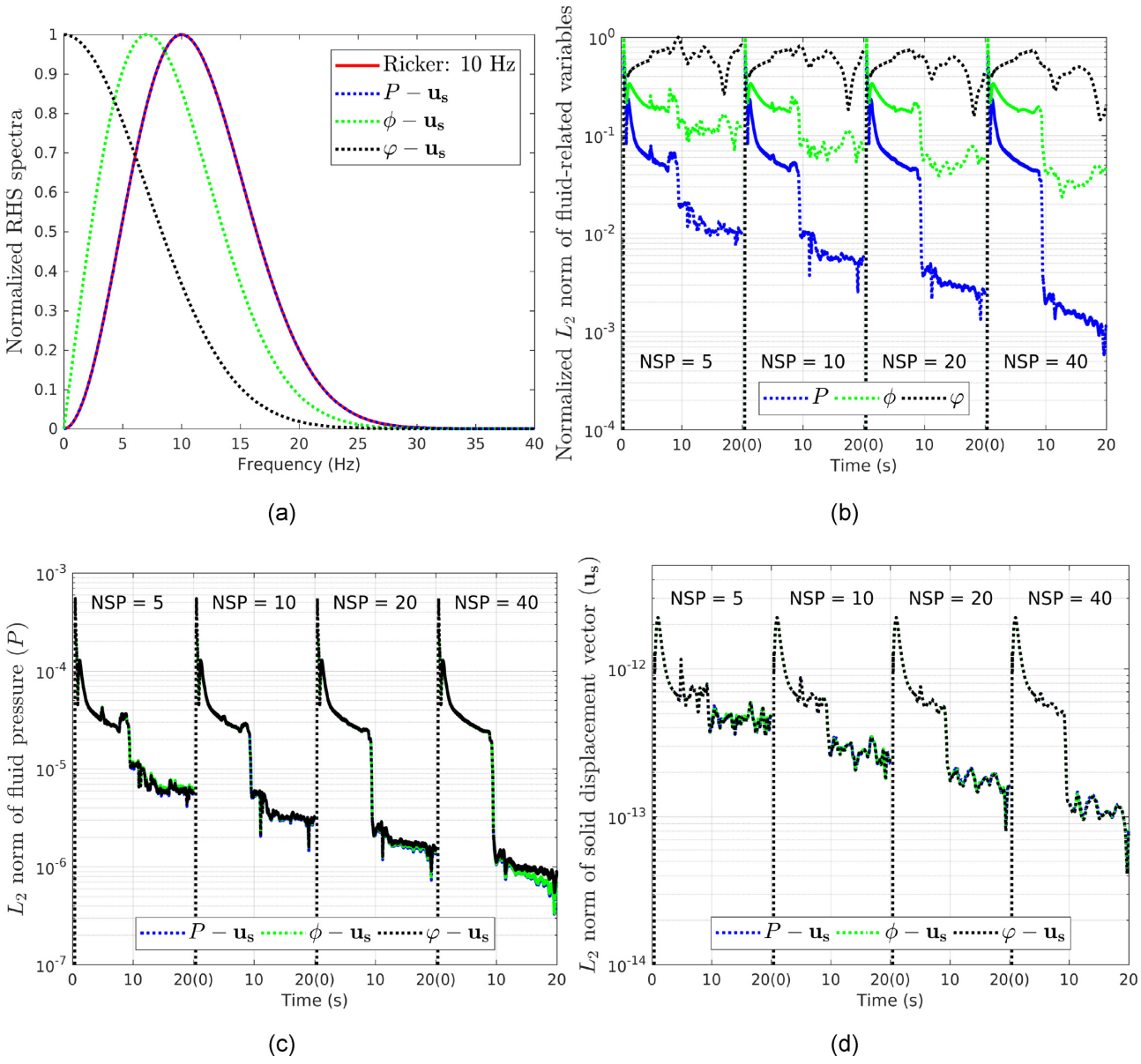

Figure 3. Absorption evaluation of sponge layers in $P - \mathbf{u}_s$, $\phi - \mathbf{u}_s$ and $\varphi - \mathbf{u}_s$ formulations. (a) Spectrum illustration of three different right-hand side (RHS) terms used in the acoustic wave equation, where a Ricker wavelet with 10 Hz peak frequency serves as the source-time function and its spectrum is plotted in red as a reference for comparison, (b) absorbing effectiveness of fluid-related variables (P, ϕ and φ) in three formulations, (c) absorbing effectiveness of the fluid pressure (P), (d) absorbing effectiveness of the solid displacement vector ($\mathbf{u}_s$). We use the L_2 norm of wavefield variables to measure the wave energy decay with respect to time in both fluid and solid domains, namely $\frac{\|P\|^2}{\|P\|^2_{\max}}$, $\frac{\|\phi\|^2}{\|\phi\|^2_{\max}}$ and $\frac{\|\varphi\|^2}{\|\varphi\|^2_{\max}}$ in (b), $\|P\|^2$ in (c) and $\|\mathbf{u}_s\|^2$ in (d). NSP: number of sponge elements.

Table 4. Comparison of the elapsed time and memory consumption for $P - \mathbf{u}_s$, $\phi - \mathbf{u}_s$ and $\varphi - \mathbf{u}_s$ systems. Shared-memory OpenMP is applied for parallelization with 32 threads.

	Elapsed time (s)	Memory (MB)
$P - \mathbf{u}_s$ system	650.75	445.64
$\phi - \mathbf{u}_s$ system	929.27	445.70
$\varphi - \mathbf{u}_s$ system	628.10	445.64

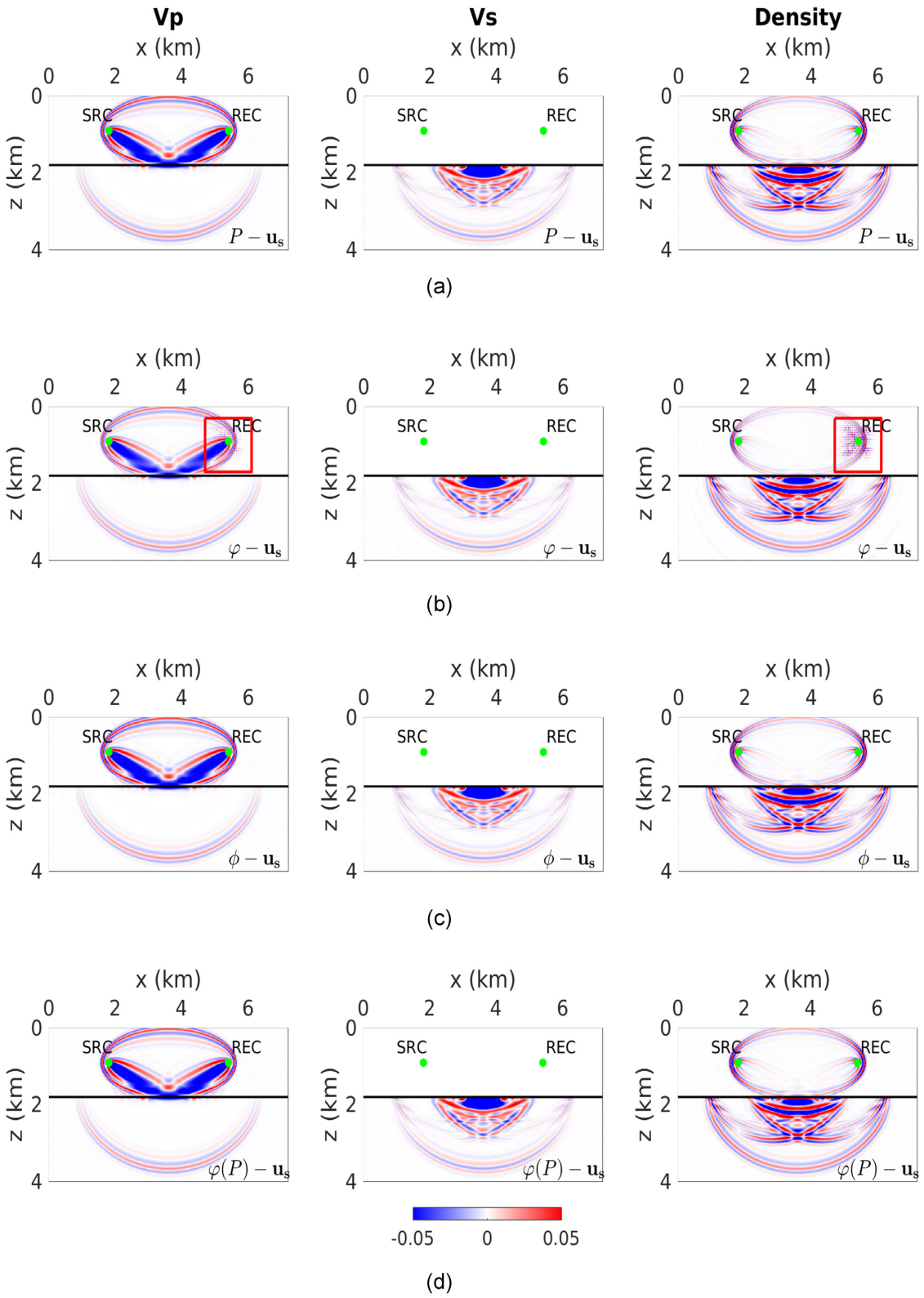

Figure 4. Comparison of the acoustic–elastic coupled gradient kernels (V_p: *P*-wave velocity, V_s: *S*-wave velocity and density) computed using 4 different approaches. (a) $P - \mathbf{u}_s$ formulation based approach, (b) $\varphi - \mathbf{u}_s$ formulation based approach, (c) $\phi - \mathbf{u}_s$ formulation based approach, (d) hybrid approach: the forward wavefield from $\varphi - \mathbf{u}_s$ formulation and the adjoint wavefield from the adjoint system of $P - \mathbf{u}_s$ formulation. The source (SRC) and receiver (REC) denoted by green dots are both in the fluid domain. Two red squares in (b) delineate the high-frequency noise on the receiver side, which is caused by using an adjoint source built by the double time-derivative of the data residual.

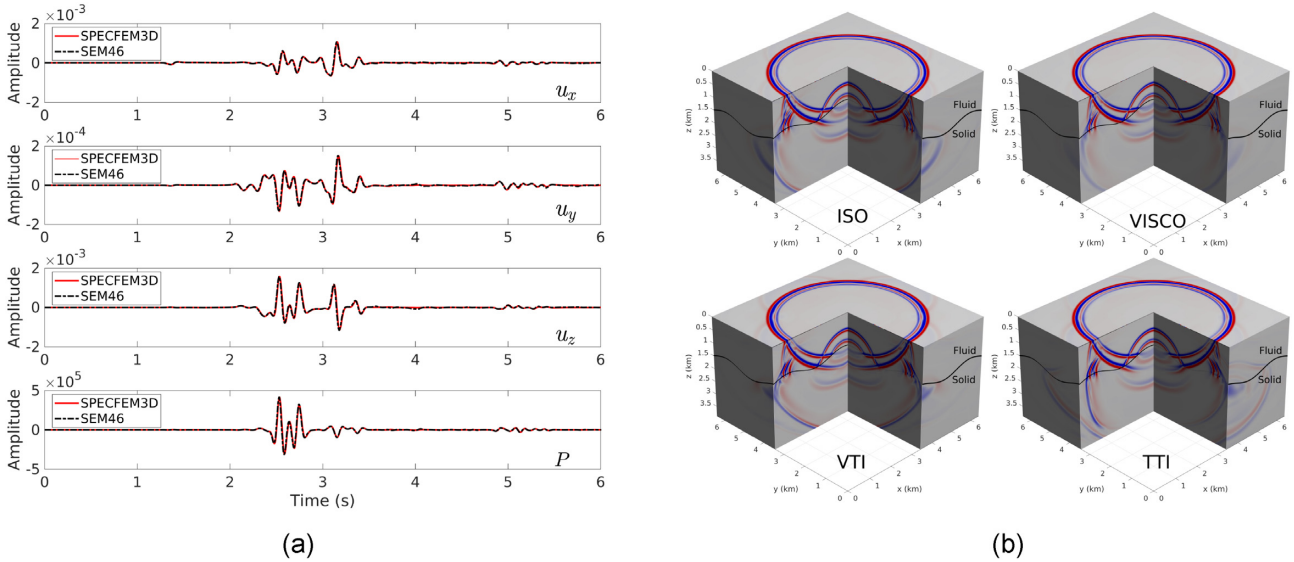

Figure 5. 3-D modelling results in the bi-layered models with a sinusoidal fluid–solid interface. (a) Seismogram comparison with results from SPECFEM3D (Peter *et al.* 2011) when the solid domain is a perfectly elastic isotropic medium, where the receiver is located at the fluid–solid interface with offsets of 2.8 and 0.1 km in the x- and y-directions. (b) Snapshot comparison of z-component displacements in the cases of isotropic, viscous-isotropic, VTI and TTI solid domains, respectively.

Seismic Imaging at eXploration scale), which is a time-domain (visco-)elastic wave-equation modelling and full waveform inversion package developed within the framework of SEISCOPE (Brossier & Trinh 2017; Trinh *et al.* 2019). To account for the real environment of marine seismic exploration, the fluid free-surface boundary condition has been applied at the model top during the implementation. Based on the physical parameters listed in Table 3, we first perform the modelling test in the 3-D bi-layered models. The same pressure source as in the 2-D test is located in the middle of x–y plane at 1 km depth below the sea level, and the receiver line is located on the seabed along the x-direction with a constant y-offset of 0.1 km. The corresponding fluid–solid coupled modelling results are shown in Fig. 5. As a validation, we choose a single trace whose x-offset is 2.8 km, and compare its 4C ocean-bottom data with results produced by SPECFEM3D (Peter *et al.* 2011) in the isotropic case. An excellent agreement can be observed in Fig. 5(a). Fig. 5(b) illustrates snapshots of the acoustic–elastic coupled modelling in the cases of isotropic, viscous-isotropic, VTI and TTI solid domains, respectively, which reveals its applicability in dealing with different kinds of media. Secondly, to demonstrate the feasibility of this hybrid approach in the 3-D gradient building, we calculate the acoustic–elastic coupled gradient kernels in the 3-D bi-layered model which has the same model parameters and perturbations as illustrated in the 2-D test. Because the free-surface boundary condition is applied in the 3-D gradient building, the resulting gradient kernels (Fig. 6) reveal a wider azimuth illumination contributed by the free-surface related multiples.

For the high performance computing (HPC) aspect of the 3-D fluid–solid coupled FWI engine, a conventional domain-decomposition strategy based on the same number of elements (same size of submesh) for each domain does not yield an appropriate load balancing. The reason is that different wave equations are involved in each part of the mesh in the fluid–solid coupled problem, therefore, the computational complexity for each element is not equivalent, depending on the domain it belongs to.

We compare the elapsed time of the fully acoustic modelling, the fully elastic modelling and new developed fluid–solid coupled modelling without any load-balanced optimization (‘without LB’) in Fig. 7(a). A rough evaluation yields a factor around 3 between the computational complexities of acoustic modelling and elastic modelling. Therefore, for the fluid–solid coupled problem, the fluid domain governed by the acoustic wave equation has less computation to perform. Consequently, domains in the fluid part wait for domains in the solid part to finish their computation, and the overall ‘time-to-solution’ is driven by the elements in the solid domain. This complexity ratio can be used to optimize the domain-decomposition strategy by weighting each element in the decomposition, proportionally to the amount of expected computation. This leads to an optimized domain decomposition with more acoustic elements in subdomains to achieve the load balancing over domains, and consequently shorten the elapsed time significantly (see two lines labelled with ‘with LB’ in Fig. 7a). The scalability of this load-balanced fluid–solid coupled engine is evaluated by calculating the relative parallel efficiency

$$\epsilon = \frac{P^{\text{ref}}}{P}\frac{T_P^{\text{ref}}}{T_P}, \tag{31}$$

where P is the number of process, T_P is the elapsed time using P processes, and P^{ref} and T_P^{ref} correspond to the number of process and elapsed time at the reference point (here we choose $P^{\text{ref}} = 32$ and 256 for two different clusters, namely DAHU and SWAN platforms). As shown in Fig. 7(b), $\epsilon = 1$ indicates a linear scaling, and we observe efficiencies over 0.95 and 0.72 on these two clusters, respectively. In addition, our implementation considers an additional constraint for the domain partitioning in order to avoid the fluid–solid interface to match a domain boundary. Thus, there is no need of the message passing interface (MPI) communication in the computation of coupling condition terms.

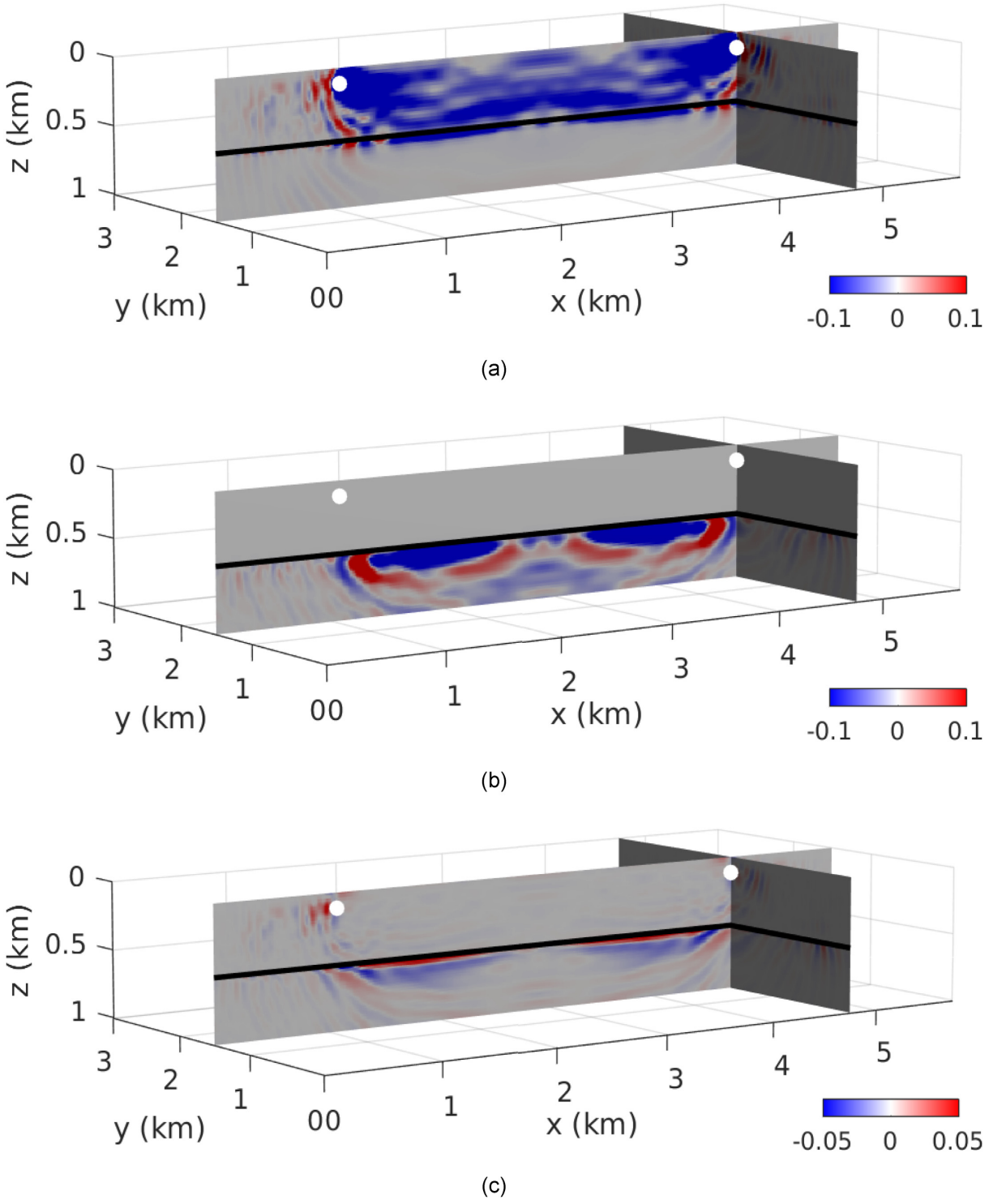

Figure 6. 3-D acoustic–elastic coupled gradient kernels computed in a hybrid way: the incident wavefield from $\varphi - \mathbf{u}_s$ system and the adjoint wavefield from the adjoint-state equation of $P - \mathbf{u}_s$ system. The parametrization is *P*-wave velocity (a), *S*-wave velocity (b) and density (c). The fluid and solid domains are separated by the flat seabed (black line), and the vertical cross-section through source (white dot on the left-hand side) and receiver (white dot on the right-hand side) is extracted.

5 FWI SYNTHETIC CASE STUDIES

In this section, we apply our fluid–solid coupled FWI engine into two synthetic case studies to highlight its feasibility and capability in the high-resolution multiparameter reconstruction. The first case study is an exploration-scale problem based on a 3-D extended Marmousi-II model (Fig. 8a), and the second one is a large 3-D deep-water crustal-scale problem based on the model shown in Fig. 8(b) which was designed to represent the offshore subduction environment of Nankai Trough in Japan (Górszczyk & Operto 2021).

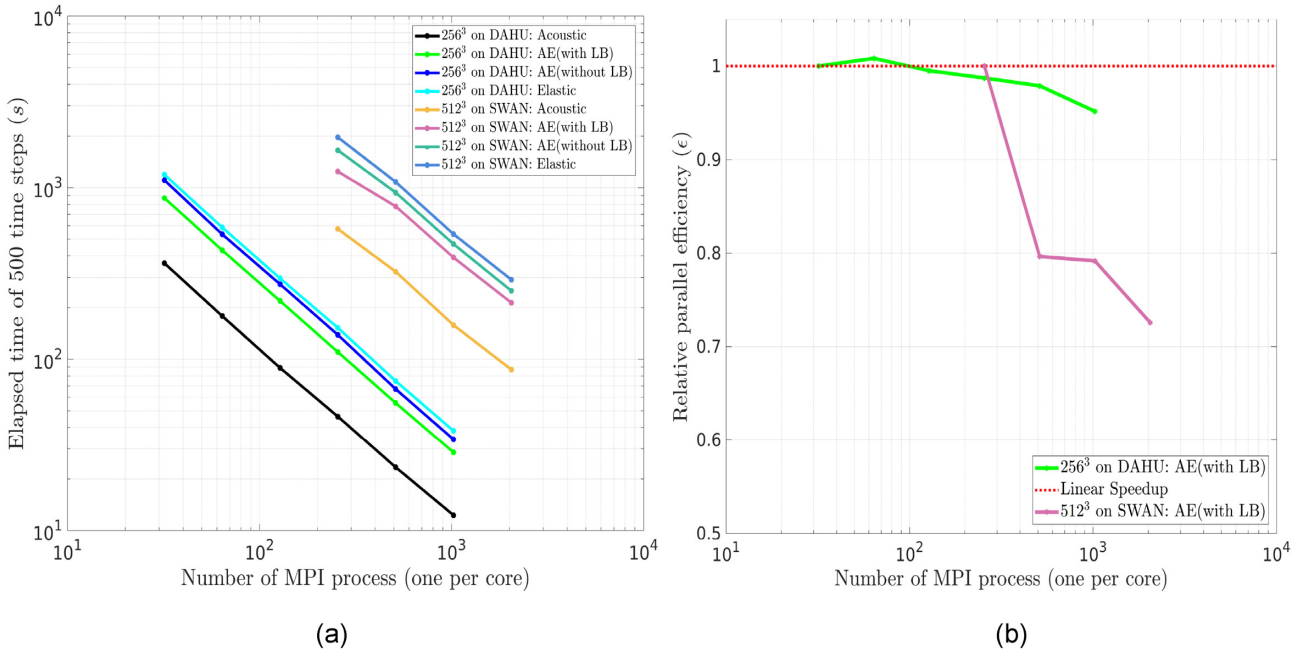

Figure 7. Efficiency tests on cubic models with 256^3 and 512^3 elements using two Intel-Xeon Skylake CPU architectures: DAHU platform from University Grenoble Alpes and SWAN platform from CRAY Marketing Partner Network (*https://partners.cray.com*). (a) Elapsed time comparison of the fully acoustic, fully elastic and fluid–solid coupled modelling (with and without load-balanced optimization), (b) estimation of relative parallel efficiency ϵ for the fluid–solid coupled modelling with the load-balanced optimization from (a).

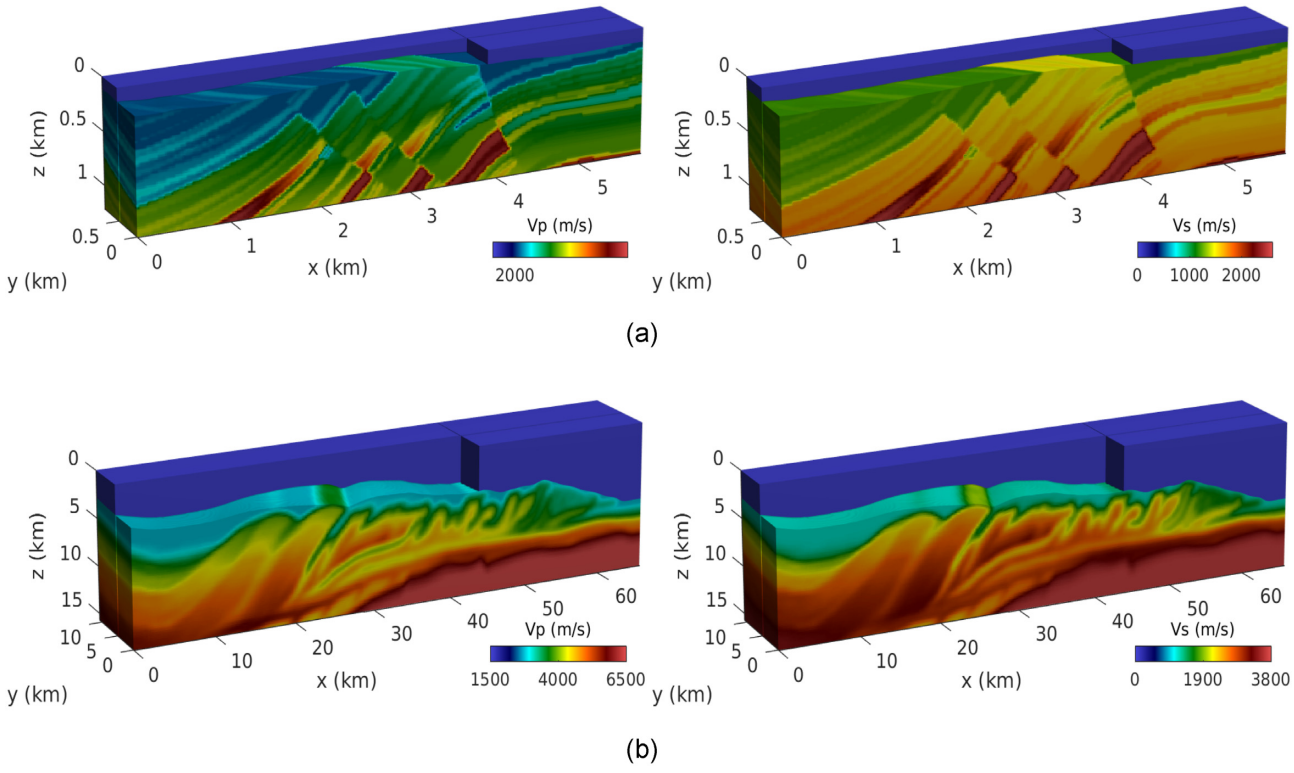

Figure 8. 3-D Marmousi-II velocity model (a) and the truncated GO_3D_OBS crustal-scale velocity model (b) used in the fluid–solid coupled FWI tests. Note that models vary in all three directions and have uneven seabeds. V_p: *P*-wave velocity, V_s: *S*-wave velocity.

5.1 3-D Marmousi-II model

5.1.1 Case study design

The Marmousi model is a 2-D marine structural model widely used in the test of seismic imaging and velocity model building techniques. Its elastic version has been developed by Martin *et al.* (2006) and named as Marmousi-II model. Our first FWI synthetic case study will be performed on a 3-D extended version of the Marmousi-II model. It is obtained by an extension along the y-direction with an angle of 45°, and an uneven seabed is added to replace the original flat one (see Fig. 8a). For clarity, we extract the slices at the seabed, the depth of $z = 0.62$ km and along the crossline direction with $y = 0.42$ km in Fig. 9. Unlike the original Marmousi-II model, the Poisson's ratio of this new model has been changed to be around 0.25 to avoid very low S-wave velocities in the sediments. The main geological characteristic of this model is the distributed steep thrust faults in the centre of the model, and our targets are those small hydrocarbon reservoirs that are embedded in the thrust fault system. For the quality control (QC) measurement, two wells across the faulted trap gas sands are considered (see two white lines marked W1 and W2 in Fig. 9).

Three different datasets are considered for better understanding the behaviour of the fluid–solid coupled FWI engine:

(i)Pressure data from a standard streamer acquisition (Streamer).
(ii)Pressure data from an OBC acquisition (OBC-P).
(iii)3C displacement data from the same OBC acquisition (OBC-3C).

We show the precise geometry of the streamer and OBC acquisitions as follows:

(i) A towed streamer acquisition along 2 shot lines (38 shots in total, every 300 m in the inline and crossline directions), in which each shot is recorded by 9 streamers with streamer separation of 50 m and maximum offset of 5.8 km in the acquisition direction as shown in Fig. 10(a)
(ii) An OBC acquisition with 18 shooting lines covering the whole $x - y$ plane (separation is 50 m) and 2 ocean-bottom cables (38 4C receivers in total, every 300 m in the inline and crossline directions) as shown in Fig. 10(b).

Those datasets are generated by the forward modelling part of the proposed engine, with a constant element-size mesh (but vertically deformed to conform the seabed variation) and a 10 Hz Ricker wavelet as the source-time function.

The initial V_p and V_s are smoothed from the true models and illustrated in Fig. 11. A similar smoothed density model is used in both observed data generation and inversion. The conventional frequency-filtered multiscale strategy (Bunks *et al.* 1995) is used in the inversion to mitigate the cycle-skipping effect, and the maximum frequency we invert is 20 Hz. The V_p and V_s models are inverted simultaneously for each dataset with the same inversion process, except that a source-receiver reciprocity is applied to the OBC dataset for decreasing the computational cost. Reciprocity relation makes it possible to interchange the role of receivers and sources in the seismic modelling, so as to benefit from the lower number of receivers. The detailed parameter settings and computational costs are listed in Table 5, and we can find that for 3C data (OBC-3C), CPU cores are required three times as much as the inversion on single component data (Streamer and OBC-P). It is because 3C geophones are viewed as 3C sources in the source–receiver reciprocity, leading to the number of source tripled in the FWI.

5.1.2 Data fit

Figs 12 and 13 show the final data fit of pressure and 3C displacement in three different datasets, in which the synthetic data of the reconstructed model are plotted in blue and red with 40 per cent transparency, while the observed data are plotted in white and black. From it, we can find an almost perfect fit between the synthetic data and the observed data in terms of phase and amplitude for all three datasets (no white, red and blue colours can be observed at the final stage). To evaluate these data-fits quantitatively, we calculate the relative difference between the synthetic data and the observed data over three datasets, namely 2.25 per cent for the streamer dataset, 2.70 per cent for the OBC-P dataset and 2.86 per cent for the OBC-3C dataset, indicating that the proposed fluid–solid coupled FWI engine successfully retrieves over 97 per cent wave information from three different types of data for the model reconstruction.

5.1.3 Streamer and OBC-P data inversion results

For the streamer and OBC-P datasets, the pressure data recorded by hydrophones in the water only contain P waves due to no S waves in the water, and the S-wave information mainly appears in terms of AVO effects on the primary P-wave reflection phases (the converted P waves are usually much weaker than it). According to the comparison of the pressure data at the initial and final stages for both datasets, we can easily find the energy redistribution of P waves at the far offset from the initial stage to the final stage (indicated by the black arrows in Fig. 12). It reveals the information of the S wave has been extracted indirectly through the amplitude variations of P waves according to the AVO effect. Their corresponding reconstructed models of V_p and V_s are shown in Figs 14 and 15, respectively. As expected, due to a wide-azimuth coverage and long offset, OBC acquisition seems to efficiently mitigate the footprints and artefacts observed in the reconstructed models from the streamer acquisition, and recovers more structure details in both V_p and V_s models (see Figs 14b and 15b where only the pressure is inverted).

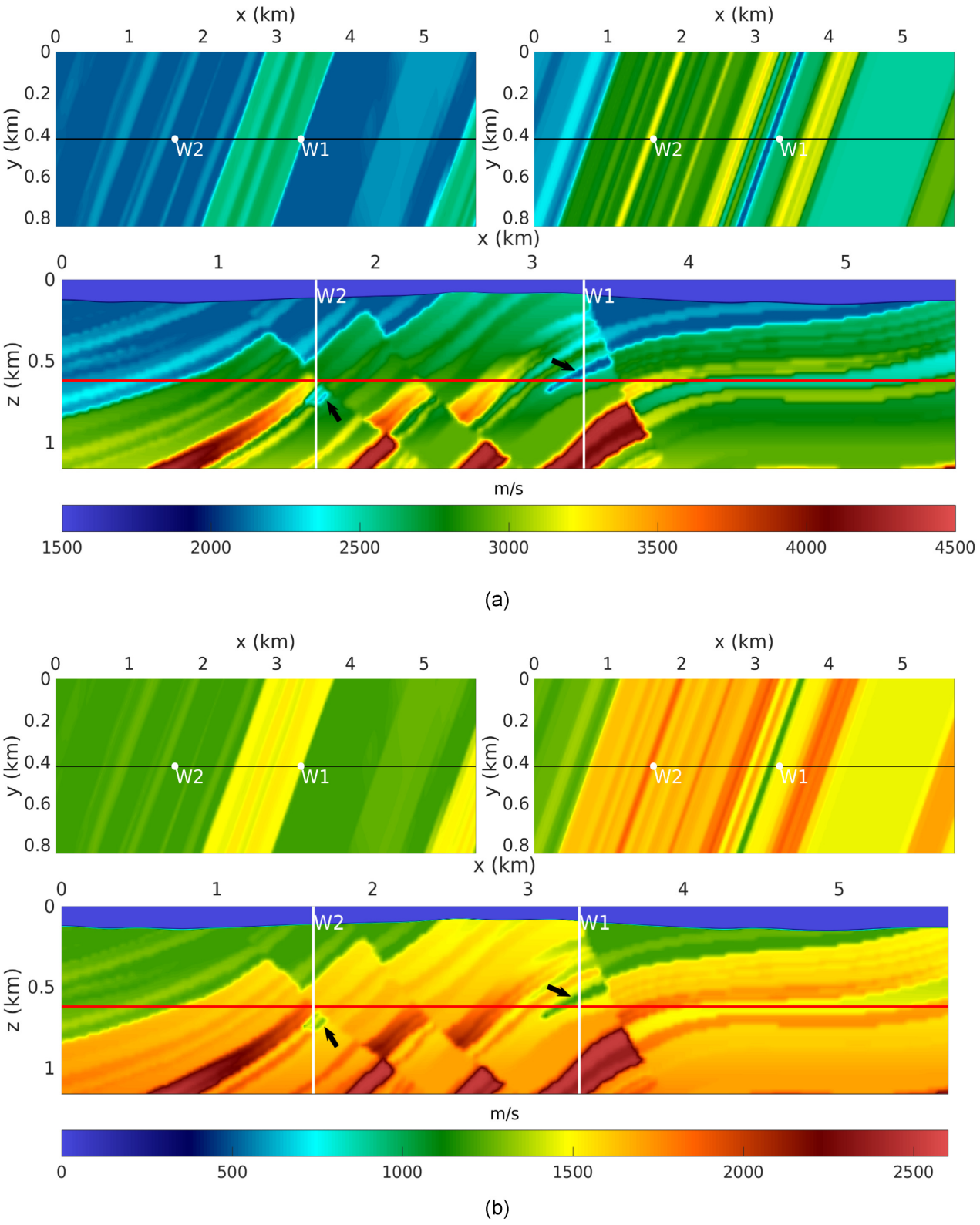

Figure 9. Velocity slices of 3-D Marmousi-II model. (a) V_p, (b) V_s. In each figure, the slices at seabed, $z = 0.62$ km (red line) and $y = 0.42$ km (black line) are shown. W1 and W2 are the wells across two faulted gas traps (indicated by black arrows), respectively.

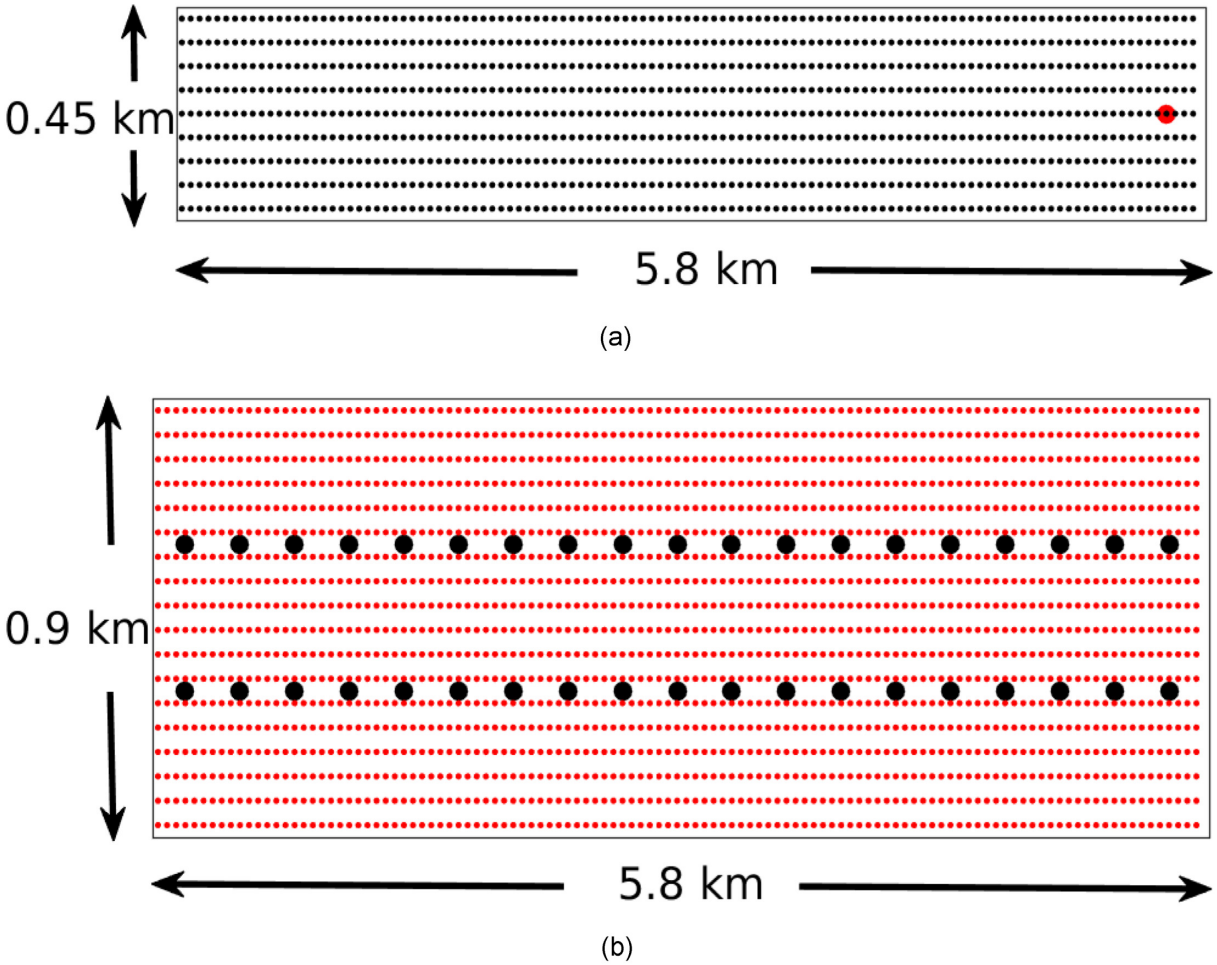

Figure 10. Acquisition geometry in the $X-Y$ plane for a single streamer vessel (a) and ocean-bottom cables (b). The red and black dots indicate the shot and receiver locations, respectively.

5.1.4 OBC-3C data inversion result

Different from the hydrophone data, both *P* and *S* waves are recorded in the OBC-3C dataset, since 3C geophones are located on the solid seabed. As shown in Fig. 13, the converted *P*-to-*S* energy can be clearly observed in the horizontal displacement components (indicated by the black arrows in Figs 13a and b), in particular to the *y*-component displacement in which converted *S* waves are dominant. Thanks to this direct recording of *S* wave information, the fluid–solid coupled FWI based on the 3C displacement dataset produces a superior *S*-wave velocity reconstruction, in which all the structure details are almost totally recovered (Fig. 15c). However, for its reconstructed *P*-wave velocity, there is no significant improvement as in the *S*-wave velocity reconstruction, when comparing with the *P*-wave velocity obtained from the OBC-P dataset (see Figs 14b and c).

5.1.5 Quality control

The vertical profiles of V_p and V_s depicted in Fig. 16 are presented for a further comparison of the FWI results from three datasets in the aspect of reservoir characterization. We can see the gas trap indicated by the black arrow at location W1 is clearly recovered from all three datasets, and a higher resolution is obtained from the reconstructed S-wave velocity model due to a smaller wavelength of S-wave compared with P-wave wavelength. For the vertical profile at location W2, it passes through two adjacent gas traps (two low velocity anomalies indicated by black arrows). However, the reconstructed V_s model from the streamer acquisition identifies them into one gas trap. The reconstructed V_s model from the OBC acquisition (either pressure or 3C displacement dataset) makes a proper distinction between them (see the low velocity anomaly indicated by the blue arrow in Fig. 16b).

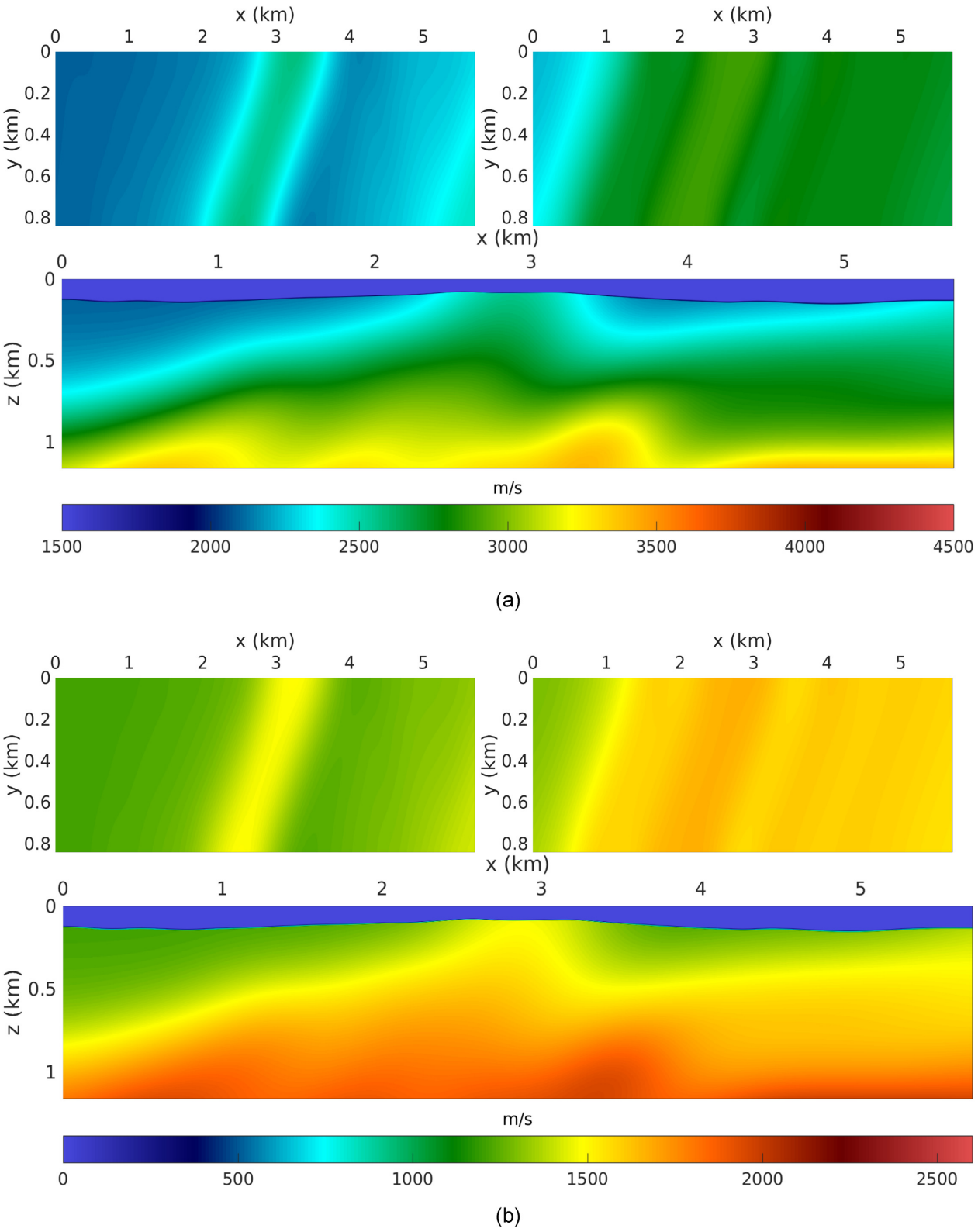

Figure 11. Initial velocity models used in the FWI of 3-D Marmousi-II model. (a) V_p, (b) V_s. In each figure, the slices at seabed, $z = 0.62$ km and $y = 0.42$ km are shown.

Table 5. Summary of parameter settings and computational costs in the fluid–solid coupled FWI of 3-D Marmousi-II model and GO_3D_OBS model. The frequency bands for 3-D Marmousi-II model are : 0 − 5 Hz (Band 1), 0 − 10 Hz (Band 2), 0 − 20 Hz (Band 3); the frequency bands for GO_3D_OBS model are : 0 − 0.5 Hz (Band 1), 0 − 1 Hz (Band 2) and 0 − 2 Hz (Band 3). Those tests are run on Jean Zay (HPE SGI 8600 supercomputer from IDRIS, national computing centre for the CNRS) with Intel Cascade Lake CPU architecture (2.5G Hz, 40 cores per node).

Model	Mesh ($x \times y \times z$)	Element size (m)	NT	Iterations	Data type	Cores	Run time (hr)		
							Band 1	Band 2	Band 3
3-D Marmousi-II	102 × 21 × 24	60	12 000	60 × 3	Streamer	1520	3.85	3.90	4.21
					OBC-P	1520	3.81	4.12	4.17
					OBC-3C	4560	3.64	4.02	4.25
GO_3D_OBS	112 × 20 × 32	600	10 000	60 × 3	OBN-P	1600	2.18	2.43	2.44
					OBN-3C	4800	1.90	2.42	2.55

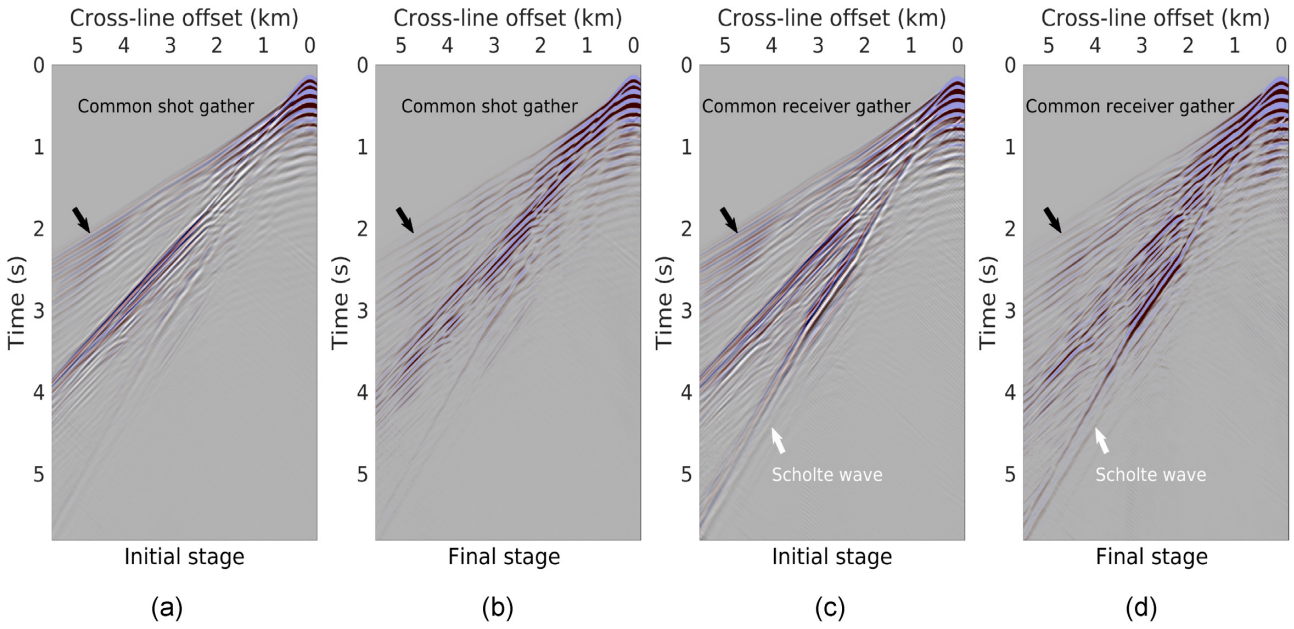

Figure 12. Pressure data-fit comparison at the initial and final stages in the streamer acquisition (a and b) and the OBC acquisition (c and d), respectively. The synthetic data (plotted in blue-red with 40 per cent transparency) are superimposed onto the observed data (plotted in white-black), and a perfect fit can be observed at the final stage (no white, red and blue colours). The black arrows indicate the energy redistribution of *P* wave at the far offset from the initial stage to the final stage. The white arrows highlight the event of Scholte wave propagating along the seabed.

5.2 GO_3D_OBS crustal-scale model

5.2.1 Case study design

In the second FWI synthetic case study, we consider the application of fluid–solid coupled FWI engine on the reconstruction of GO_3D_OBS subduction zone model (Fig. 8b). Essentially, this is a seismology-scale problem with a sparse acquisition and low-frequency data in contrast to the exploration-scale test mentioned above. The reconstruction of S-wave velocity or Vp/Vs ratio is very important in the subduction environment, since it can give a lot of information about the presence of fluids which migrate along the plate interface, the branches of the splay faults, or in the subduction channel. Such information contributes to the analysis of potential earthquakes. The extracted V_p and V_s slices at the seabed, the depth of $z = 12$ km and along the crossline direction with $y = 4.8$ km are shown in Fig. 17. It can be seen that the region of this model is quite large with x, y and z dimensions of 64.8 km × 9.6 km × 14.55 km, and therefore it has a wider range of Poisson's ratio from 0.21 to 0.38 in the subsurface. In addition, compared with the 3-D extended Marmousi-II model, its water depth has a significant variation from 2.55 km to 8.35 km, which might produce strong and complex free-surface related multiples leading to difficulties in the FWI. Our aim is to reconstruct the complex geometry of accretionary wedge illustrated in the $x - z$ section in Fig. 17.

Here we use a ocean-bottom node (OBN) acquisition consisting of 20 4C receiver nodes distributed sparsely on the seabed with spacing intervals of 8.5 km in the inline direction and 2.5 km in the crossline direction, and 16 shooting lines (1720 shots in total) covering the whole

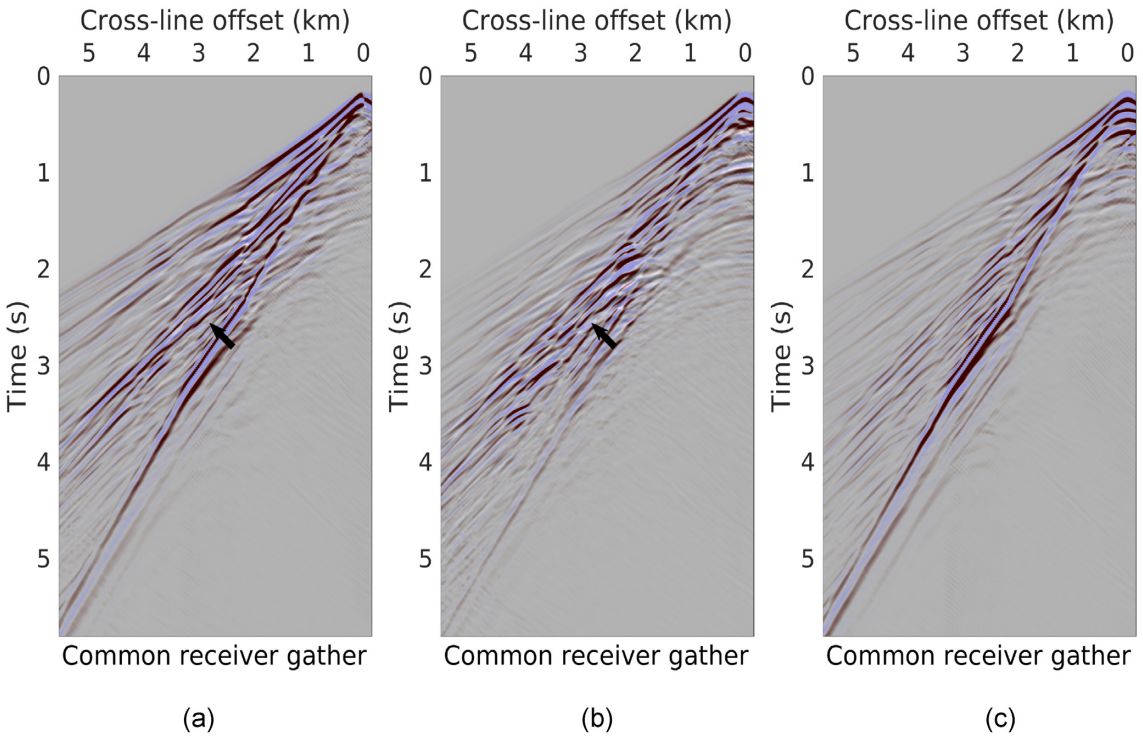

Figure 13. Comparison of 3C displacement data at the final stage in the OBC acquisition: (a) u_x, (b) u_y and (c) u_z. The synthetic data (plotted in blue-red with 40 per cent transparency) are superimposed onto the observed data (plotted in white-black), and a perfect fit can be observed (no white, red and blue colours). The black arrows indicate the converted *P*-to-*S* energy recorded from the horizontal components, which is dominant in the *y* component (b).

$x - y$ plane with a separation of 0.6 km as presented in the seabed slice in Fig. 17. Again, we use the forward modelling part to generate the observed 4C data (pressure + 3C displacement) with a constant element-size mesh (but vertically deformed to conform the seabed variation) and a 1 Hz Ricker wavelet as the source-time function. The same workflow for the fluid–solid coupled FWI is run on the pressure dataset and 3C displacement dataset, respectively, from the low-frequency band ($\leq$0.5 Hz) to the high-frequency band ($\leq$2 Hz). The detailed parameter settings and computational costs are listed in Table 5 as well.

5.2.2 *Inversion results*

Figs 18 and 19 compare the initial and reconstructed models of V_p and V_s, respectively. For this study, we also invert V_p and V_s simultaneously, and use a smooth density model computed from the initial V_p with Gardner's relation (Gardner *et al.* 1974) in both observed data generation and inversion. Although the overall velocity structures of V_p and V_s have been significantly improved compared with the initial status, the updates of V_p from both pressure and 3C displacement are only limited to the shallow region and missing small-scale structures. By contrast, the reconstructed V_s models are updated in a deeper region and exhibit more structure details, especially for the V_s obtained from 3C displacement dataset that recovers most of the features of the true V_s model (see the fine-scale sediments in the subducting channel indicated by black arrows in Fig. 19c). A comparison of the data fit in Fig. 20 reveals that a perfect data matching is achieved at the near offset for both pressure and 3C displacement datasets. However, we can observe a significant discrepancy at the far offset where P-waves are dominant (events with red and blue colours delineated by white circles), which explains a poor recovery of V_p in the deep region. The reason that data fit at the near and far offsets are inconsistent in the FWI is probably related to the unbalanced energy contribution of P- and S-waves in the L_2-based misfit function. We display the data residuals of pressure and 3C displacement computed on the initial models (see Fig. 21), and their low-pass frequency-filtered results are used as the adjoint sources at the first FWI stage. Because the low-pass frequency filtering only changes the signal frequency band not the original energy distribution of P- and S-waves, we can use these data residuals to reveal the energy contribution of P- and S-waves in the misfit function. As shown in Fig. 21, for the FWI in both pressure and 3C displacement datasets, the near-offset traces are dominant in the contribution of misfit function ensuring a good reconstruction of the shallow region, whereas the contribution of far-offset traces (P-wave dominant) delineated by blue and red lines is nearly ignorable leading to the lack of enough information in the deep region reconstruction of V_p. For the traces in the intermediate-offset region (converted P-to-S waves dominant) delineated by black and blue lines, its contribution is strengthened in the 3C displacement dataset compared with the pressure dataset, which makes it possible to better constrain the V_s reconstruction.

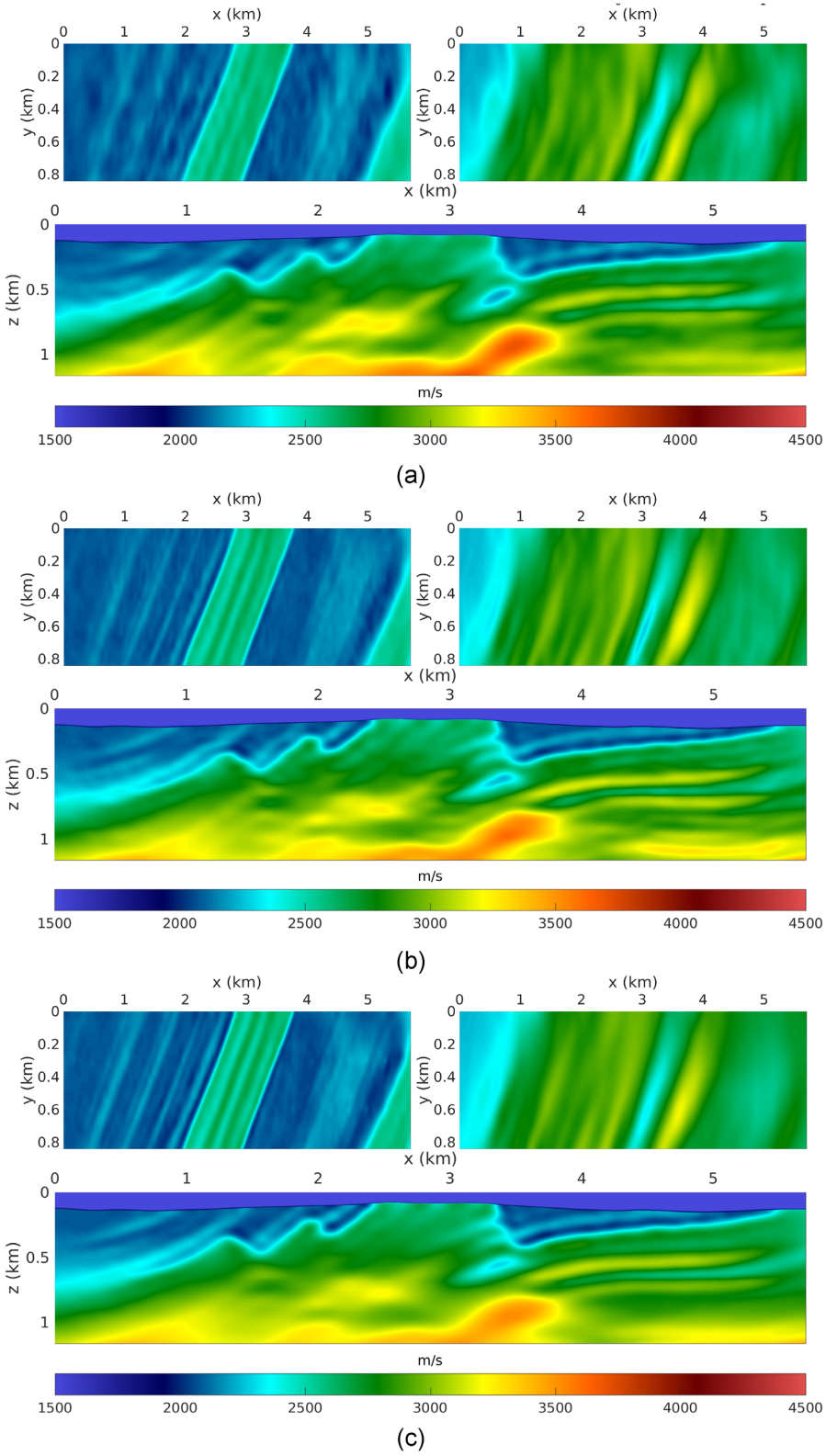

Figure 14. Inversion results of V_p by using the streamer acquisition (a), OBC acquisition with pressure data only (b) and OBC acquisition with 3C displacement data (c). In each figure, the slices at seabed, $z = 0.62$ km and $y = 0.42$ km are shown.

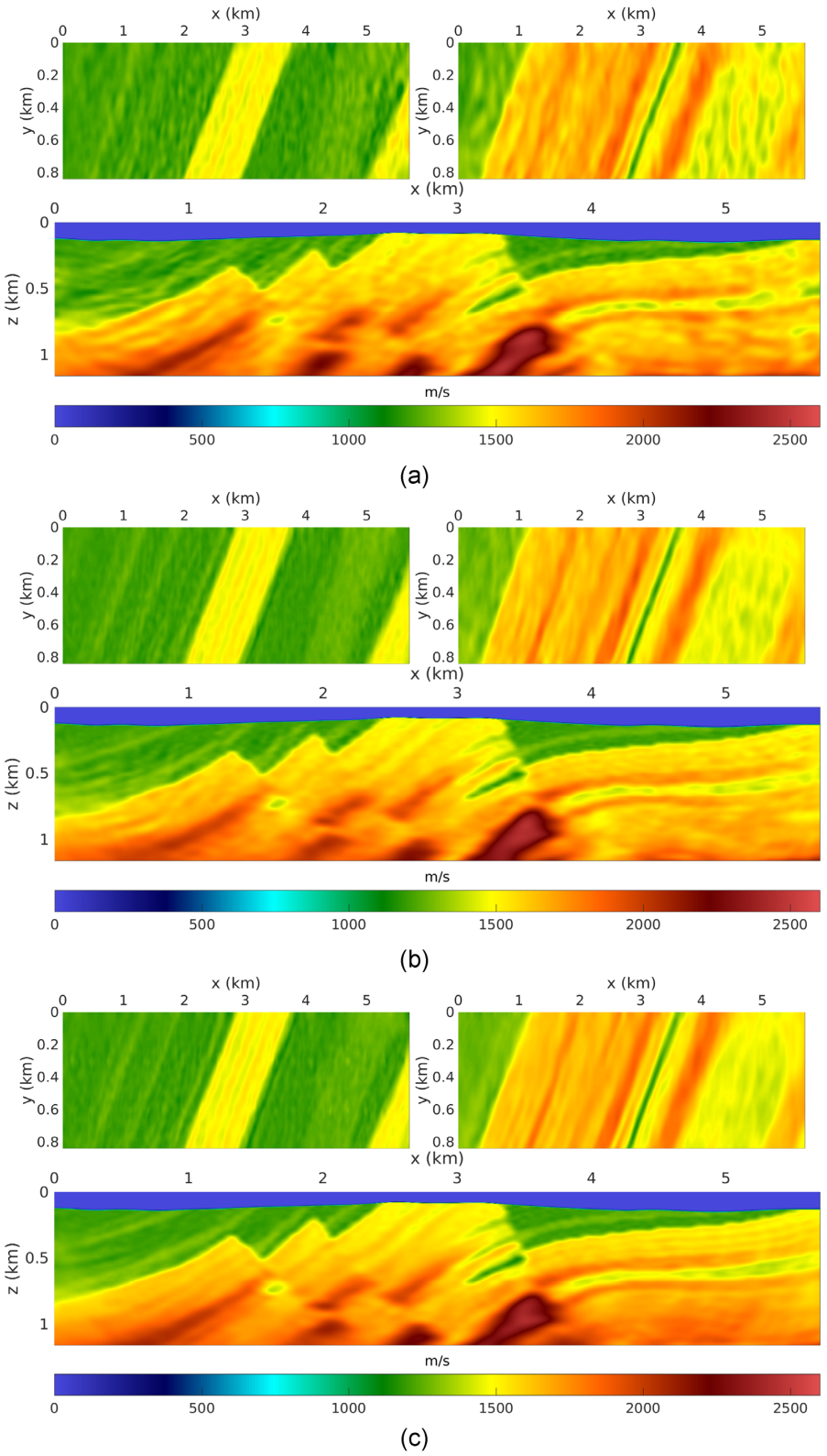

Figure 15. Inversion results of V_s by using the streamer acquisition (a), OBC acquisition with pressure data only (b) and OBC acquisition with 3C displacement data (c). In each figure, the slices at seabed, $z = 0.62$ km and $y = 0.42$ km are shown.

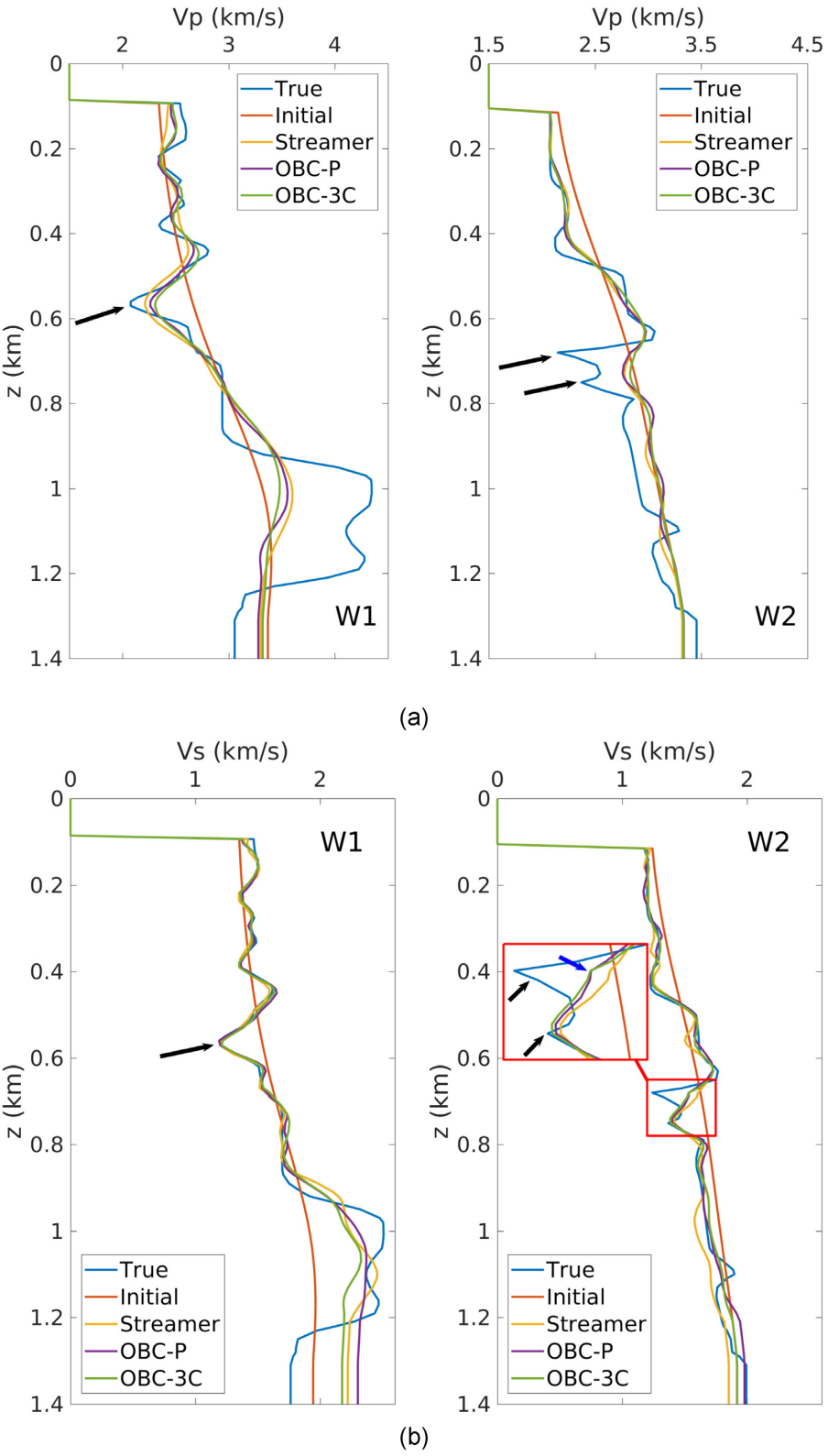

Figure 16. Vertical profiles for comparing the V_p (a) and V_s (b) inversion results at well locations W1 and W2. The low-velocity anomalies indicated by black arrows are gas traps. The inset in (b) zooms in the red square region which delineates two adjacent gas traps.

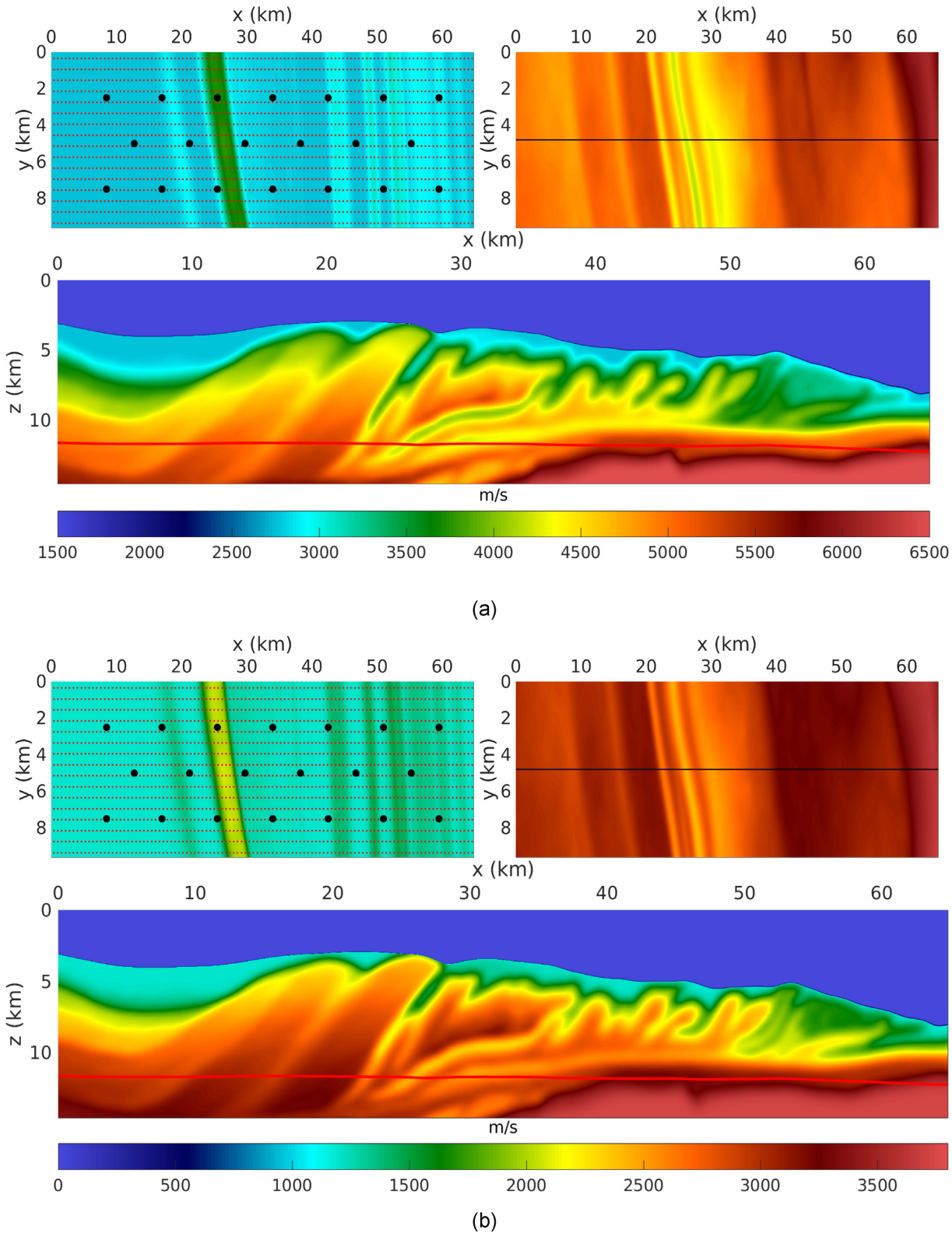

Figure 17. Velocity slices of GO_3D_OBS model. (a) V_p, (b) V_s. In each figure, the slices at seabed, $z = 12$ km (red line) and $y = 4.8$ km (black line) are shown. The distribution of ocean-bottom nodes (black dots) and shots (red dots) are depicted on the seabed slice.

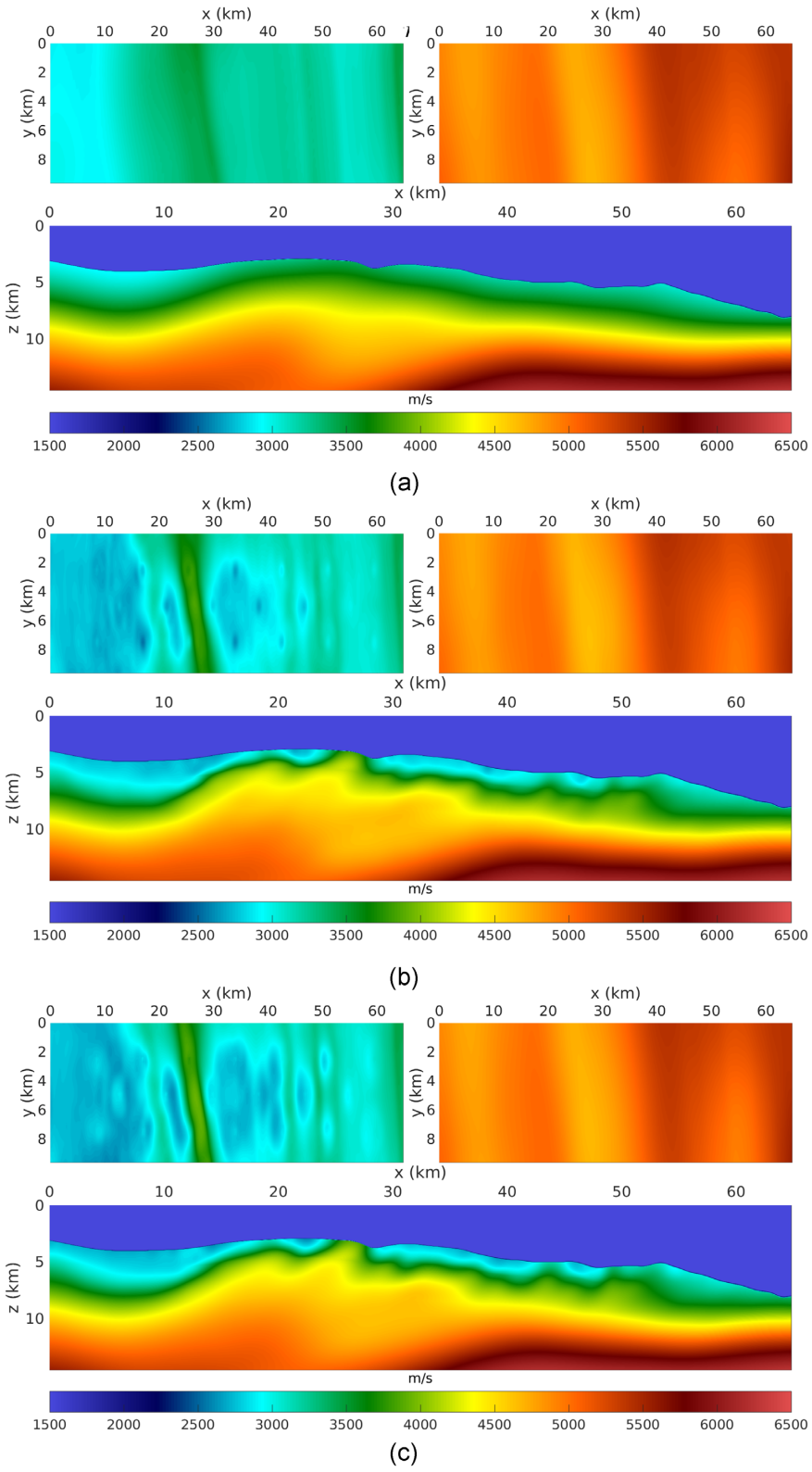

Figure 18. V_p slices of the initial model (a), reconstructed model using OBN acquisition with pressure data only (b), reconstructed model using OBN acquisition with 3C displacement data (c). In each figure, the slices at seabed, $z = 12$ km and $y = 4.8$ km are shown.

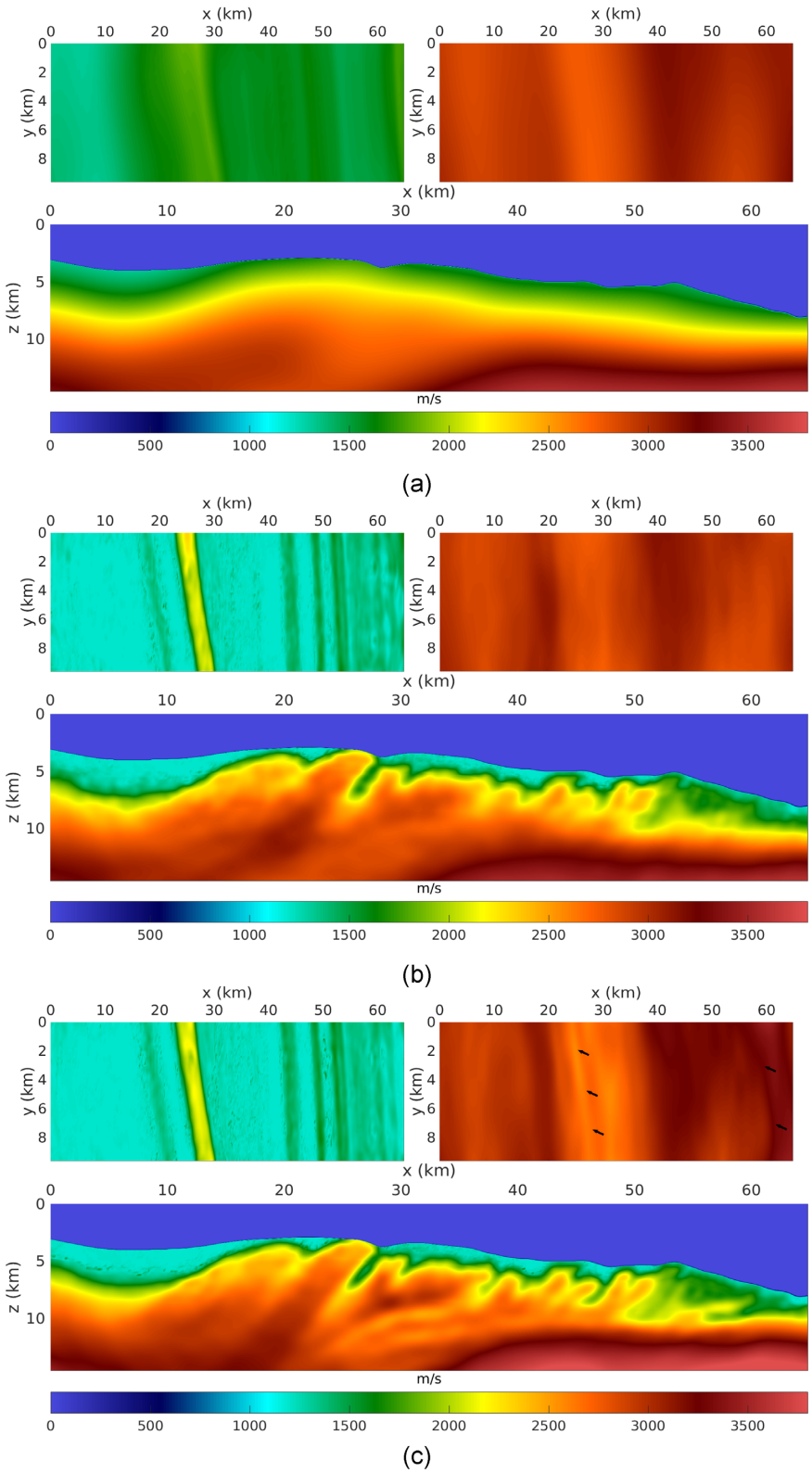

Figure 19. V_s slices of the initial model (a), reconstructed model using OBN acquisition with pressure data only (b), reconstructed model using OBN acquisition with 3C displacement data (c). In each figure, the slices at seabed, $z = 12$ km and $y = 4.8$ km are shown.

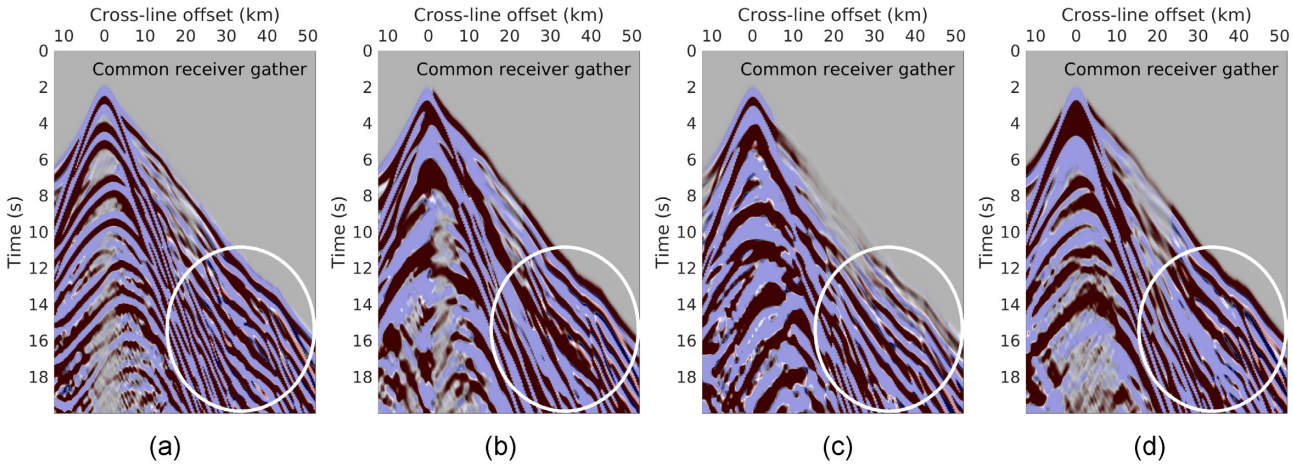

Figure 20. Data-fit comparison at the final stage: (a) the pressure dataset (OBN-P), (b)-(d) the 3C displacement data (OBN-3C) corresponding to u_x, u_y and u_z, respectively. The synthetic data (plotted in blue-red with 40 per cent transparency) are superimposed onto the observed data (plotted in white-black), and they are normalized trace by trace. The regions delineated by white circles show the mismatch of the synthetic data and the observed data at the far offset (red and blue colours can be observed), where the P-wave energy is dominant.

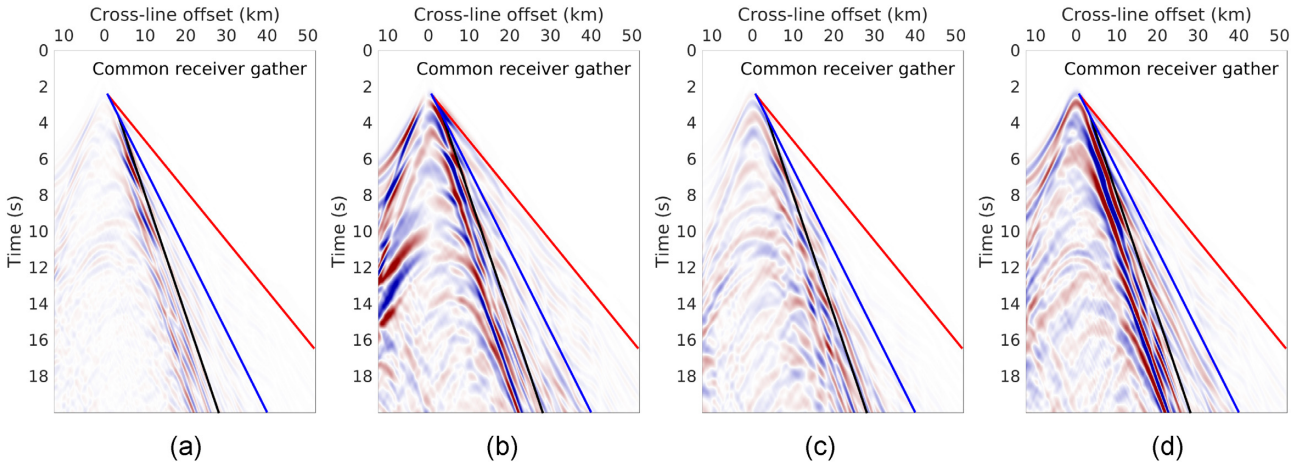

Figure 21. Comparison of the residuals (serving as the adjoint sources) of two datasets at the initial stage: (a) the pressure data (OBN-P), (b)–(d) the 3C displacement data (OBN-3C) corresponding to u_x, u_y and u_z, respectively. Here two regions corresponding to intermediate- and far-offsets are highlighted: the intermediate-offset region between black and blue lines is dominated by converted *P*-to-*S* waves, and the far-offset region between blue and red lines is dominated by the *P* waves.

6 CONCLUSIONS

Our study presents a new efficient fluid–solid coupled FWI parallel engine for modelling and inverting the multicomponent ocean-bottom seismic data, where the acoustic–elastic coupled wave-equation system is introduced to simulate the elastic effects in synthetic data. Consequently, the forward problem and the definition of the associated FWI problem are developed within the framework of the acoustic–elastic coupled wave-equation system. According to different wavefield variables used in the fluid domain, we recast and investigate 4 acoustic–elastic coupled formulations: $P - \mathbf{u}_s$ formulation, $\varphi - \mathbf{u}_s$ formulation, $\phi - \mathbf{u}_s$ formulation and $\mathbf{u}_f - \mathbf{u}_s$ formulation. From the aspect of wave propagation modelling, both theoretical analysis and SEM-based 2-D numerical tests reveal that the $\varphi - \mathbf{u}_s$ formulation has a better performance in terms of accuracy and computational efficiency than the other three formulations, due to its precise representation of the fluid–solid boundary condition and explicit time-marching scheme. In the FWI part, we put forward a hybrid approach for the gradient building. This approach involves the $\varphi - \mathbf{u}_s$ formulation for the incident wavefield simulation and the $P - \mathbf{u}_s$ formulation for the adjoint wavefield simulation. It achieves the possibility of using the same explicit solver in the solution of both forward and adjoint problems. The feasibility test of this hybrid approach in 2-D also shows its another advantage of eliminating the unwanted high-frequency noise on the receiver side in the computation.

The 3-D implementation of this SEM-based fluid–solid coupled FWI engine is accomplished within the framework of the SEISCOPE SEM46 code. For the parallel computing aspect, a load-balanced domain-decomposition strategy is proposed. Various simulations with increasing complexity are presented, including the wave modelling in isotropic elastic, anisotropic elastic (VTI and TTI) and viscoelastic media, for an accuracy, efficiency and applicability evaluation. The constructed gradient kernels from this engine reveal the model parameters

can be inferred from data through the contribution of different waves, such as the diving wave, reflected wave and *P*-to-*S* converted wave that supports the *S*-wave velocity reconstruction. In particular, by applying the free-surface boundary condition, the resulting gradient kernels show a wider azimuth illumination contributed by the free-surface related multiples. Finally, we provide two FWI synthetic case studies on exploration-scale and crustal-scale models to confirm the feasibility of the proposed SEM-based 3-D fluid–solid coupled FWI engine in the high-resolution multiparameter reconstruction. Their results demonstrate a significant resolution improvement can be obtained from the reconstruction of the *S*-wave velocity model, especially for the use of 3C geophone dataset in the ocean-bottom acquisition. In addition, in the inversion with pressure data only, the proposed SEM-based 3-D fluid–solid coupled FWI engine also shows its ability of reconstructing the *S*-wave velocity through AVO effects from the amplitude variation of *P* waves.

Future work will be devoted to (1) further applications of this 3-D SEM-based fluid–solid coupled FWI engine in several ocean-bottom seismic case studies, including high-quality synthetic data and field data; (2) investigation on the inversion workflow of multicomponent data (4C data), such as the hierarchical strategies over different data components and the alternative multicomponent misfit function, so as to quantify both *P*- and *S*-wave velocities accurately; (3) extensions of the engine to reconstruct more parameters (such as density, anisotropy and attenuation parameters) and efficiency improvement based on GPU accelerated architecture.

ACKNOWLEDGEMENTS

The work leading to these results has received funding from the European Union's Horizon 2020 research and innovation programme under the ENERXICO project, grant agreement No. 828947. This work was also partially funded by the SEISCOPE consortium (*http://seiscope2.osug.fr*), sponsored by AKERBP, CGG, CHEVRON, EQUINOR, EXXON-MOBIL, JGI, SHELL, SINOPEC, SISPROBE and TOTAL. This work was granted access to the HPC resources of the Dahu platform of the CIMENT infrastructure (*https://ciment.ujf-grenoble.fr*), which is supported by the Rhône-Alpes region (GRANT CPER07_13 CIRA), the OSUG@2020 labex (reference ANR10 LABX56) and the Equip@Meso project (reference ANR-10-EQPX-29-01) of the programme Investissements d'Avenir supervised by the Agence Nationale pour la Recherche, Cray Marketing Partner Network (*https://partners.cray.com*) and the HPC resources of CINES/IDRIS/TGCC under the allocation 046091 made by GENCI. This work benefited from many fruitful discussions with Yang Li, Marwan Irnaka and Nishant Kamath. We thank the associate editor Carl Tape and two reviewers Qiancheng Liu and Josep de la Puente for their careful reading and insightful comments.

7 DATA AVAILABILITY

Data and code associated with this research belong to the SEISCOPE consortium. Any request related to the materials availability needs to be addressed to Romain Brossier (romain.brossier@univ-grenoble-alpes.fr).

REFERENCES

Agudo, O.C., da Silva, N.V., Warner, M. & Morgan, J., 2018. Acoustic full-waveform inversion in an elastic world, *Geophysics,* **83**(3), 1–62, doi:10.1190/geo2017-0063.1.

Agudo, Ò.C., da Silva, N.V., Stronge, G. & Warner, M., 2020. Mitigating elastic effects in marine 3-D full-waveform inversion, *Geophys. J. Int.,* **220**(3), 2089–2104.

Amestoy, P., Brossier, R., Buttari, A., L'Excellent, J.-Y., Mary, T., Métivier, L., Miniussi, A. & Operto, S., 2016. Fast 3D frequency-domain full waveform inversion with a parallel Block Low-Rank multifrontal direct solver: application to OBC data from the North Sea, *Geophysics,* **81**(6), R363–R383.

Antonietti, F.P., Bonaldi, F. & Mazzieri, I., 2020. Simulation of 3D elasto-acoustic wave propagation based on a discontinuous galerkin spectral element method, *Int. J. Numer. Methods Eng.,* **121**(10), 2206–2226, doi:10.1002/nme.6305.

Barnes, C. & Charara, M., 2009. The domain of applicability of acoustic full-waveform inversion for marine seismic data, *Geophysics,* **74**(6), WCC91–WCC103.

Brossier, R. & Trinh, P.T., 2017. *SEM46 Manual Version 2.1,* SEISCOPE Consortium.

Bunks, C., Salek, F.M., Zaleski, S. & Chavent, G., 1995. Multiscale seismic waveform inversion, *Geophysics,* **60**(5), 1457–1473.

Cao, J., Brossier, R. & Métivier, L., 2020a. 3D acoustic-(visco)elastic coupled formulation and its spectral-element implementation on a Cartesian-based hexahedral mesh, in *Proceedings of the SEG Technical Program Expanded Abstracts 2020,* pp. 2643–2647.

Cao, J., Brossier, R. & Métivier, L., 2020b. Comparison of formulations for representing the fluid-solid coupling using the spectral element method, in *Proceedings of the 82nd Annual EAGE Meeting,* Amsterdam, Expanded Abstracts, pp. 1–5.

Cerjan, C., Kosloff, D., Kosloff, R. & Reshef, M., 1985. A nonreflecting boundary condition for discrete acoustic and elastic wave equations, *Geophysics,* **50**(4), 2117–2131.

Chaljub, E. & Valette, B., 2004. Spectral element modelling of three-dimensional wave propagation in a self-gravitating earth with an arbitrarily stratified outer core, *Geophys. J. Int.,* **158**(1), 131–141.

De Basabe, J.D. & Sen, M.K., 2015. A comparison of finite-difference and spectral-element methods for elastic wave propagation in media with a fluid-solid interface, *Geophys. J. Int.,* **200**(1), 278–298.

de la Puente, J., Ferrer, M., Hanzich, M., Castillo, J.E. & Cela, J.M., 2014. Mimetic seismic wave modeling including topography on deformed staggered grids, *Geophysics,* **79**(3), T125–T141.

Diaz, J. & Ezziani, A., 2008. *Gar6more 2d,* http://www.spice-rtn.org/library/software/Gar6more2D.

Everstine, G.C., 1997. Finite element formulatons of structural acoustics problems, *Comput. Struct.,* **65**(3), 307–321.

Feng, X., 2000. Analysis of finite element methods and domain decomposition algorithms for a fluid-solid interaction problem, *SIAM J. Numer. Anal.,* **38**(4), 1312–1336.

Gardner, G. H.F., Gardner, L.W. & Gregory, A.R., 1974. Formation velocity and density–the diagnostic basics for stratigraphic traps, *Geophysics,* **39,** 770–780.

Górszczyk, A. & Operto, S., 2021. GO_3D_OBS: the multi-parameter benchmark geomodel for seismic imaging method assessment and next-generation 3D survey design (version 1.0), *Geoscient. Model Dev.,* **14**(3), 1773–1799.

Górszczyk, A., Operto, S. & Malinowski, M., 2017. Toward a robust workflow for deep crustal imaging by FWI of OBS data: the eastern Nankai Trough revisited, *J. geophys. Res.,* **122**(6), 4601–4630.

Hestholm, S. & Ruud, B., 1998. 3-D finite-difference elastic wave modeling including surface topography, *Geophysics,* **63**(2), 613–622.

Hestholm, S. & Ruud, B., 2002. 3D free-boundary conditions for coordinate-transform finite-difference seismic modelling, *Geophys. Prospect.,* **50,** 463–474.

Hou, G., Wang, J. & Layton, A., 2012. Numerical methods for fluid-structure interaction—a review, *Commun. Comput. Phys.,* **12**(2), 337–377.

Kamath, N., Brossier, R., Métivier, L., Pladys, A. & Yang, P., 2021. Multi-parameter full-waveform inversion of 3D ocean-bottom cable data from the Valhall field, *Geophysics,* **86**(1), B15–B35.

Karypis, G., 2013. *METIS - A Software Package for Partitioning Unstructured Graphs, Partitioning Meshes, and Computing Fill-Reducing Orderings of Sparse Matrices - Version 5.1.0,* University of Minnesota.

Kelly, K., Ward, R., Treitel, S. & Alford, R., 1976. Synthetic seismograms—a finite-difference approach, *Geophysics,* **41,** 2–27.

Komatitsch, D., 1997. Méthodes spectrales et éléments spectraux pour l'équation de l'élastodynamique 2D et 3D en milieu hétérogène, *PhD thesis*, Institut de Géophysique du Globe de Paris.

Komatitsch, D. & Tromp, J., 1999. Introduction to the spectral element method for 3D seismic wave propagation, *Geophys. J. Int.,* **139,** 806–822.

Komatitsch, D. & Vilotte, J.P., 1998. The spectral element method: an efficient tool to simulate the seismic response of 2D and 3D geological structures, *Bull. seism. Soc. Am.,* **88,** 368–392.

Komatitsch, D., Barnes, C. & Tromp, J., 2000. Wave propagation near a fluid-solid interface: a spectral element approach, *Geophysics,* **65**(2), 623–631.

Konuk, T. & Shragge, J., 2019. 3D tensorial elastodynamics for anisotropic media, in *SEG Technical Program Expanded Abstracts 2019,* pp. 3934–3938.

Lailly, P., 1983. The seismic problem as a sequence of before-stack migrations, in *Proceedings of the Conference on Inverse Scattering: Theory and Applications,* SIAM, Philadelphia.

Lysmer, J. & Kuhlemeyer, R., 1969. Finite dynamic model for infinite media, *J. Eng. Mech. Div.,* **95**(EM4), 859–877.

Martin, G.S., Wiley, R. & Marfurt, K.J., 2006. Marmousi2: an elastic upgrade for Marmousi, *Leading Edge,* **25**(2), 156–166.

Maver, K.G., 2011. Ocean bottom seismic: strategic technology for the oil industry, *First Break,* **29**(12), 75–80.

Mönkölä, S., 2011. Numerical simulation of fluid-structure interaction between acoustic and elastic waves, *PhD thesis*, University of Jyväskylä.

Morgan, J., Warner, M., Bell, R., Ashley, J., Barnes, D., Little, R., Roele, K. & Jones, C., 2013. Next-generation seismic experiments: wide-angle, multi-azimuth, three-dimensional, full-waveform inversion, *Geophys. J. Int.,* **195,** 1657–1678.

Nocedal, J., 1980. Updating quasi-Newton matrices with limited storage, *Math. Comput.,* **35**(151), 773–782.

Operto, S., Virieux, J., Dessa, J.X. & Pascal, G., 2006. Crustal imaging from multifold ocean bottom seismometers data by frequency-domain full-waveform tomography: application to the eastern Nankai Trough, *J. geophys. Res.,* **111**(B09306), doi:10.1029/2005JB003835.

Operto, S., Miniussi, A., Brossier, R., Combe, L., Métivier, L., Monteiller, V., Ribodetti, A. & Virieux, J., 2015. Efficient 3-D frequency-domain mono-parameter full-waveform inversion of ocean-bottom cable data: application to Valhall in the visco-acoustic vertical transverse isotropic approximation, *Geophys. J. Int.,* **202**(2), 1362–1391.

Park, K. & Felippa, C., 1980. Partitioned transient analysis procedures for coupled-field problems: accuracy analysis, *J. appl. Mech.,* **47**(4), 919–926.

Pellegrini, F., 2018. *PT-SCOTCH and libPTSCOTCH 6.0 User's Guide - Version 6.0.5,* Université Bordeaux.

Peter, D. *et al.*, 2011. Forward and adjoint simulations of seismic wave propagation on fully unstructured hexahedral meshes, *Geophys. J. Int.,* **186**(2), 721–739.

Plessix, R.E., 2006. A review of the adjoint-state method for computing the gradient of a functional with geophysical applications, *Geophys. J. Int.,* **167**(2), 495–503.

Prieux, V., Brossier, R., Operto, S. & Virieux, J., 2013a. Multiparameter full waveform inversion of multicomponent OBC data from Valhall. Part 1: imaging compressional wavespeed, density and attenuation, *Geophys. J. Int.,* **194**(3), 1640–1664.

Prieux, V., Brossier, R., Operto, S. & Virieux, J., 2013b. Multiparameter full waveform inversion of multicomponent OBC data from Valhall. Part 2: imaging compressional and shear-wave velocities, *Geophys. J. Int.,* **194**(3), 1665–1681.

Reinarz, A. *et al.*, 2020. ExaHyPE: an engine for parallel dynamically adaptive simulations of wave problems, *Comput. Phys. Commun.,* **254,** 107251.

Ross, M.R., Sprague, M.A., Felippa, C.A. & Park, K.C., 2009. Treatment of acoustic fluid-structure interaction by localized lagrange multipliers and comparison to alternative interface-coupling methods, *Comput. Methods Appl. Mech. Eng.,* **198**(9-12), 986–1005.

Sears, T., Singh, S. & Barton, P., 2008. Elastic full waveform inversion of multi-component OBC seismic data, *Geophys. Prospect.,* **56**(6), 843–862.

Sears, T.J., Barton, P.J. & Singh, S.C., 2010. Elastic full waveform inversion of multicomponent ocean-bottom cable seismic data: application to Alba Field, U.K. North Sea, *Geophysics,* **75**(6), R109–R119.

Sethi, H., Shragge, J. & Tsvankin, I., 2021. Mimetic finite-difference coupled-domain solver for anisotropic media, *Geophysics,* **86**(1), T45–T59.

Sirgue, L., Barkved, O.I., Dellinger, J., Etgen, J., Albertin, U. & Kommedal, J.H., 2010. Full waveform inversion: the next leap forward in imaging at Valhall, *First Break,* **28,** 65–70.

Sun, Y.-C., Zhang, W., Xu, J.-K. & Chen, X., 2017. Numerical simulation of 2-D seismic wave propagation in the presence of a topographic fluid–solid interface at the sea bottom by the curvilinear grid finite-difference method, *Geophys. J. Int.,* **210**(3), 1721–1738.

Tarantola, A., 1984. Inversion of seismic reflection data in the acoustic approximation, *Geophysics,* **49**(8), 1259–1266.

Tarrass, I., Giraud, L. & Thore, P., 2011. New curvilinear scheme for elastic wave propagation in presence of curved topography, *Geophys. Prospect.,* **59**(5), 889–906.

Trinh, P.T., Brossier, R., Métivier, L., Tavard, L. & Virieux, J., 2019. Efficient 3D time-domain elastic and viscoelastic full waveform inversion using a spectral-element method on flexible Cartesian-based mesh, *Geophysics,* **84**(1), R75–R97.

Virieux, J., 1986. P-SV wave propagation in heterogeneous media: velocity-stress finite difference method, *Geophysics,* **51,** 889–901.

Virieux, J. & Operto, S., 2009. An overview of full waveform inversion in exploration geophysics, *Geophysics,* **74**(6), WCC1–WCC26.

Virieux, J., Asnaashari, A., Brossier, R., Métivier, L., Ribodetti, A. & Zhou, W., 2017. An introduction to full waveform inversion, in *Encyclopedia of Exploration Geophysics,* pp. R1–1-R1-40, eds Grechka, V. & Wapenaar, K., Society of Exploration Geophysics.

Walker, C., 2020. Ocean bottom node technology—what next?, in *Proceedings of the Second EAGE Marine Acquisition Workshop,* Vol. 2020, pp. 1–3, European Association of Geoscientists & Engineers.

Wang, P., Zhang, Z., Mei, J., Lin, F. & Huang, R., 2019. Full-waveform inversion for salt: a coming of age, *Leading Edge,* **38**(3), 204–213.

Yao, J., Guasch, L., Warner, M., Lin, T. & Percak-Dennett, E., 2020. Geophysical data and gradient translation using deep neural networks, in *SEG Technical Program Expanded Abstracts 2020,* pp. 1725–1729.

Zhang, W., Zhang, Z. & Chen, X., 2012. Three-dimensional elastic wave numerical modelling in the presence of surface topography by a collocated-grid finite-difference method on curvilinear grids, *Geophys. J. Int.,* **190**(1), 358–378.

Zhu, J., Popovics, J.S. & Schubert, F., 2004. Leaky Rayleigh and Scholte waves at the fluid–solid interface subjected to transient point loading, *J. acoust. Soc. Am.,* **116**(4), 2101–2110.

APPENDIX: ADJOINT SYSTEM OF THE $P - U_S$ FORMULATION

According to the Lagrange multiplier method, we define the associated Lagrangian as

$$
\begin{aligned}
L\left(P, \mathbf{u}_s; \mu^{(P)}, \mu_0, \mu_1, \beta, \boldsymbol{\lambda}, \boldsymbol{\lambda}_0, \boldsymbol{\lambda}_1, \boldsymbol{\alpha}\right) = & \frac{1}{2}\sum\nolimits_{s,r}\int_0^T \alpha_s\left(\mathbf{S}_{s,r}\mathbf{W}_P(t) - \mathbf{d}_P^{\text{obs}}(t)\right)^2 + \beta_s\left(\mathbf{S}_{s,r}\mathbf{W}_{\mathbf{u}}(t) - \mathbf{d}_{\mathbf{u}}^{\text{obs}}(t)\right)^2 \mathrm{d}t \\
& - \int_0^T\int_{\Omega_f} \mu^{(P)}(\mathbf{x},t)\cdot\left\{\frac{1}{\kappa}\partial_{tt}P(\mathbf{x},t) - \nabla\cdot\left(\frac{1}{\rho_f}\nabla P(\mathbf{x},t)\right) - \frac{1}{\kappa}P_f\right\}\mathrm{d}V\mathrm{d}t \\
& - \int_0^T\int_{\Omega_s} \boldsymbol{\lambda}(\mathbf{x},t)\cdot\left\{\rho_s\partial_{tt}\mathbf{u}_s(\mathbf{x},t) - \nabla\cdot\boldsymbol{\sigma}(\mathbf{x},t) - \mathbf{f}_s\right\}\mathrm{d}V\mathrm{d}t \\
& - \int_{\Omega_f}\mu_0(\mathbf{x},0)\cdot P(\mathbf{x},0)\,\mathrm{d}V - \int_{\Omega_f}\mu_1(\mathbf{x},0)\cdot\partial_t P(\mathbf{x},0)\,\mathrm{d}V \\
& - \int_{\Omega_s}\boldsymbol{\lambda}_0(\mathbf{x},0)\cdot\mathbf{u}_s(\mathbf{x},0)\,\mathrm{d}V - \int_{\Omega_s}\boldsymbol{\lambda}_1(\mathbf{x},0)\cdot\partial_{\mathbf{t}}\mathbf{u}_s(\mathbf{x},0)\,\mathrm{d}V \\
& - \int_0^T\int_{\Gamma_{fs}}\beta(\mathbf{x},t)\cdot\left\{\partial_{tt}\mathbf{u}_s(\mathbf{x},t)\cdot\mathbf{n} + \frac{1}{\rho_f}\nabla P(\mathbf{x},t)\cdot\mathbf{n}\right\}\mathrm{d}S\mathrm{d}t \\
& - \int_0^T\int_{\Gamma_{fs}}\boldsymbol{\alpha}(\mathbf{x},t)\cdot\left\{\boldsymbol{\sigma}_s(\mathbf{x},t)\cdot\mathbf{n} + P(\mathbf{x},t)\,\mathbf{n}\right\}\mathrm{d}S\mathrm{d}t,
\end{aligned}
\tag{A1}
$$

where μ_0, μ_1, $\boldsymbol{\lambda}_0$ and $\boldsymbol{\lambda}_1$ are adjoint-state variables associated with the initial conditions, and $\boldsymbol{\alpha}$ and β are adjoint-state variables associated with the fluid–solid boundary conditions.

A1 Acoustic adjoint-state equation

The derivative of eq. (A1) with respect to the wavefield variable P is

$$
\begin{aligned}
\frac{\partial L}{\partial P} = & \sum\nolimits_{s,r}\alpha_s\mathbf{S}_{s,r}^T\left(\mathbf{S}_{s,r}\mathbf{W}_P(t) - \mathbf{d}_P^{\text{obs}}(t)\right) \\
& \underbrace{- \frac{\partial}{\partial P}\left[\int_0^T\int_{\Omega_f}\mu^{(P)}(\mathbf{x},t)\cdot\left[\frac{1}{\kappa}\partial_{tt}P(\mathbf{x},t) - \nabla\cdot\left(\frac{1}{\rho_f}\nabla P(\mathbf{x},t)\right)\right]\mathrm{d}V\mathrm{d}t\right]}_{⓪} \\
& - \frac{\partial}{\partial P}\left[\int_{\Omega_f}\mu_0(\mathbf{x},0)\cdot P(\mathbf{x},0)\,\mathrm{d}V + \int_{\Omega_f}\mu_1(\mathbf{x},0)\cdot\partial_t P(\mathbf{x},0)\,\mathrm{d}V\right] \\
& - \frac{\partial}{\partial P}\left[\int_0^T\int_{\Gamma_{fs}}\left(\beta(\mathbf{x},t)\cdot\frac{1}{\rho_f}\nabla P(\mathbf{x},t)\cdot\mathbf{n} + \boldsymbol{\alpha}(\mathbf{x},t)\cdot P(\mathbf{x},t)\,\mathbf{n}\right)\mathrm{d}S\mathrm{d}t\right].
\end{aligned}
\tag{A2}
$$

By integrating twice by parts in time and space, the term ⓪ can be reformulated as

$$
⓪ = \left\{
\begin{aligned}
& \tfrac{\partial}{\partial P}\left[\int_{\Omega_f}\tfrac{\partial_t\mu^{(P)}(\mathbf{x},0)}{\kappa}P(\mathbf{x},0)\,\mathrm{d}V - \int_{\Omega_f}\tfrac{\mu^{(P)}(\mathbf{x},0)}{\kappa}\partial_t P(\mathbf{x},0)\,\mathrm{d}V\right] \\
& \quad + \tfrac{\partial}{\partial P}\left[\int_{\Omega_f}\tfrac{\mu^{(P)}(\mathbf{x},T)}{\kappa}\partial_t P(\mathbf{x},T)\,\mathrm{d}V - \int_{\Omega_f}\tfrac{\partial_t\mu^{(P)}(\mathbf{x},T)}{\kappa}P(\mathbf{x},T)\,\mathrm{d}V\right] \\
& \quad + \int_0^T\int_{\Omega_f}\tfrac{1}{\kappa}\partial_{tt}\mu^{(P)}(\mathbf{x},t) - \nabla\cdot\left(\tfrac{1}{\rho_f}\nabla\mu^{(P)}(\mathbf{x},t)\right)\mathrm{d}V\mathrm{d}t \\
& \quad + \tfrac{\partial}{\partial P}\left[-\int_0^T\int_{\Gamma_{fs}}\tfrac{1}{\rho_f}\nabla\mu^{(P)}(\mathbf{x},t)\cdot P(\mathbf{x},t)\,\mathbf{n}\mathrm{d}S\mathrm{d}t + \int_0^T\int_{\Gamma_{fs}}\tfrac{1}{\rho_f}\mu^{(P)}(\mathbf{x},t)\,\nabla P(\mathbf{x},t)\cdot\mathbf{n}\mathrm{d}S\mathrm{d}t\right].
\end{aligned}
\right.
\tag{A3}
$$

The adjoint-state variables are evaluated by

$$
\tfrac{\partial L}{\partial P} = 0.
\tag{A4}
$$

Consequently, we have

$$\begin{aligned}\frac{\partial L}{\partial P} =& \underbrace{\sum\nolimits_{s,r}\alpha_s \mathbf{S}_{s,r}^T\left(\mathbf{S}_{s,r}\mathbf{W}_P(t)-\mathbf{d}_P^{\text{obs}}(t)\right)-\int_0^T\int_{\Omega_f}\frac{1}{\kappa}\partial_{tt}\mu^{(P)}(\mathbf{x},t)-\nabla\cdot\left(\frac{1}{\rho_f}\nabla\mu^{(P)}(\mathbf{x},t)\right)\mathrm{d}V\mathrm{d}t}_{①}\\
&-\underbrace{\frac{\partial}{\partial P}\left[\int_{\Omega_f}\frac{\partial_t\mu^{(P)}(\mathbf{x},0)}{\kappa}P(\mathbf{x},0)\,\mathrm{d}V+\int_{\Omega_f}\mu_0(\mathbf{x},0)\cdot P(\mathbf{x},0)\,\mathrm{d}V\right]}_{②}\\
&-\underbrace{\frac{\partial}{\partial P}\left[-\int_{\Omega_f}\frac{\mu^{(P)}(\mathbf{x},0)}{\kappa}\partial_t P(\mathbf{x},0)\,\mathrm{d}V+\int_{\Omega_f}\mu_1(\mathbf{x},0)\cdot\partial_t P(\mathbf{x},0)\,\mathrm{d}V\right]}_{③}\\
&-\underbrace{\frac{\partial}{\partial P}\int_{\Omega_f}\frac{\mu^{(P)}(\mathbf{x},T)}{\kappa}\partial_t P(\mathbf{x},T)\,\mathrm{d}V}_{④}+\underbrace{\frac{\partial}{\partial P}\int_{\Omega_f}\frac{\partial_t\mu^{(P)}(\mathbf{x},T)}{\kappa}P(\mathbf{x},T)\,\mathrm{d}V}_{⑤}\\
&+\underbrace{\frac{\partial}{\partial P}\int_0^T\int_{\Gamma_{fs}}\left(\frac{1}{\rho_f}\nabla\mu^{(P)}(\mathbf{x},t)\cdot P(\mathbf{x},t)\,\mathbf{n}-\boldsymbol{\alpha}(\mathbf{x},t)\cdot P(\mathbf{x},t)\,\mathbf{n}\right)\mathrm{d}S\mathrm{d}t}_{⑥}\\
&-\underbrace{\frac{\partial}{\partial P}\int_0^T\int_{\Gamma_{fs}}\left(\frac{1}{\rho_f}\mu^{(P)}(\mathbf{x},t)\nabla P(\mathbf{x},t)\cdot\mathbf{n}+\beta(\mathbf{x},t)\cdot\frac{1}{\rho_f}\nabla P(\mathbf{x},t)\cdot\mathbf{n}\right)\mathrm{d}S\mathrm{d}t}_{⑦}\\
=&\ 0.\end{aligned}\tag{A5}$$

By zeroing ① to ⑦ simultaneously, we obtain the acoustic adjoint-state equations

$$\begin{aligned}&\frac{1}{\kappa}\partial_{tt}\mu^{(P)}(\mathbf{x},t)+\nabla\cdot\left(-\frac{1}{\rho_f}\nabla\mu^{(P)}(\mathbf{x},t)\right)=\sum_{s,r}\alpha_s\mathbf{S}_{s,r}^T\left(\mathbf{S}_{s,r}\mathbf{W}_P(t)-\mathbf{d}_P^{\text{obs}}(t)\right),\\
&\mu_0(\mathbf{x},0)=-\frac{1}{\kappa}\partial_t\mu^{(P)}(\mathbf{x},0),\quad \mu_1(\mathbf{x},0)=\frac{1}{\kappa}\mu^{(P)}(\mathbf{x},0),\\
&\mu^{(P)}(\mathbf{x},T)=0,\quad \partial_t\mu^{(P)}(\mathbf{x},T)=0,\\
&\boldsymbol{\alpha}(\mathbf{x},t)\cdot\mathbf{n}=\frac{1}{\rho_f}\nabla\mu^{(P)}(\mathbf{x},t)\cdot\mathbf{n},\quad \beta(\mathbf{x},t)\,\mathbf{n}=-\mu^{(P)}(\mathbf{x},t)\,\mathbf{n}.\end{aligned}\tag{A6}$$

A2 Elastic adjoint-state equation

The derivative of eq.(A1) with respect to the wavefield variable $\mathbf{u}_s$ is

$$\begin{aligned}\frac{\partial L}{\partial P} =& \sum\nolimits_{s,r}\beta_s\mathbf{S}_{s,r}^T\left(\mathbf{S}_{s,r}\mathbf{W}_{\mathbf{u}}(t)-\mathbf{d}_{\mathbf{u}}^{\text{obs}}(t)\right)-\underbrace{\frac{\partial}{\partial\mathbf{u}_s}\left[\int_0^T\int_{\Omega_s}\boldsymbol{\lambda}(\mathbf{x},t)\cdot\{\rho_s\partial_{tt}\mathbf{u}_s(\mathbf{x},t)-\nabla\cdot\boldsymbol{\sigma}(\mathbf{x},t)\}\,\mathrm{d}V\mathrm{d}t\right]}_{⓪}\\
&-\frac{\partial}{\partial\mathbf{u}_s}\left[\int_{\Omega_s}\boldsymbol{\lambda}_0(\mathbf{x},0)\cdot\mathbf{u}_s(\mathbf{x},0)\,\mathrm{d}V+\int_{\Omega_s}\boldsymbol{\lambda}_1(\mathbf{x},0)\cdot\partial_t\mathbf{u}_s(\mathbf{x},0)\,\mathrm{d}V\right]\\
&-\frac{\partial}{\partial\mathbf{u}_s}\left[\int_0^T\int_{\Gamma_{fs}}(\beta(\mathbf{x},t)\cdot\partial_{\mathbf{tt}}\mathbf{u}_s(\mathbf{x},t)\cdot\mathbf{n}_s+\boldsymbol{\alpha}(\mathbf{x},t)\cdot\boldsymbol{\sigma}_s(\mathbf{x},t)\cdot\mathbf{n}_s)\,\mathrm{d}S\mathrm{d}t\right].\end{aligned}\tag{A7}$$

By integrating twice by parts in time and space, the term ⓪ can be reformulated as

$$⓪=\left\{\begin{array}{l}\frac{\partial}{\partial\mathbf{u}_s}\left[\int_{\Omega_s}\rho_s\partial_t\boldsymbol{\lambda}(\mathbf{x},0)\cdot\mathbf{u}_s(\mathbf{x},0)\,\mathrm{d}V-\int_{\Omega_s}\rho_s\boldsymbol{\lambda}(\mathbf{x},0)\cdot\partial_t\mathbf{u}_s(\mathbf{x},0)\,\mathrm{d}V\right]\\
\quad+\frac{\partial}{\partial\mathbf{u}_s}\left[\int_{\Omega_s}\rho_s\boldsymbol{\lambda}(\mathbf{x},T)\cdot\partial_t\mathbf{u}_s(\mathbf{x},T)\,\mathrm{d}V-\int_{\Omega_s}\rho_s\partial_t\boldsymbol{\lambda}(\mathbf{x},T)\cdot\mathbf{u}_s(\mathbf{x},T)\,\mathrm{d}V\right]\\
\quad+\int_0^T\int_{\Omega_s}(\rho_s\partial_{tt}\boldsymbol{\lambda}(\mathbf{x},t)-\nabla\cdot\mathbf{T}(\mathbf{x},t))\,\mathrm{d}V\mathrm{d}t\\
\quad+\frac{\partial}{\partial\mathbf{u}_s}\left[\int_0^T\int_{\Gamma_{fs}}\mathbf{T}(\mathbf{x},t)\cdot\mathbf{n}\cdot\mathbf{u}_s(\mathbf{x},t)\,\mathrm{d}S\mathrm{d}t-\int_0^T\int_{\Gamma_{fs}}\boldsymbol{\sigma}_s(\mathbf{x},t)\cdot\mathbf{n}\cdot\boldsymbol{\lambda}(\mathbf{x},t)\,\mathrm{d}S\mathrm{d}t\right],\end{array}\right.\tag{A8}$$

where $\mathbf{T} = \mathbf{C} : \nabla\boldsymbol{\lambda}$. The adjoint-state variables are evaluated by

$$\frac{\partial L}{\partial \mathbf{u}_s} = 0. \tag{A9}$$

Consequently, we have

$$\begin{aligned}
\frac{\partial L}{\partial \mathbf{u}_s} = & \underbrace{\sum\nolimits_{s,r} \beta_s \mathbf{S}_{s,r}^T \left(\mathbf{S}_{s,r}\mathbf{W}_{\mathbf{u}}(t) - \mathbf{d}_{\mathbf{u}}^{\text{obs}}(t)\right) - \int_0^T \int_{\Omega_s} \left(\rho_s \partial_{tt}\boldsymbol{\lambda}(\mathbf{x},t) - \nabla\cdot\mathbf{T}(\mathbf{x},t)\right) \mathrm{d}V\,\mathrm{d}t}_{①} \\
& - \underbrace{\frac{\partial}{\partial \mathbf{u}_s}\left[\int_{\Omega_s} \left(\rho_s \partial_t\boldsymbol{\lambda}(\mathbf{x},0)\cdot\mathbf{u}_s(\mathbf{x},0) + \boldsymbol{\lambda}_0(\mathbf{x},0)\cdot\mathbf{u}_s(\mathbf{x},0)\right)\mathrm{d}V\right]}_{②} \\
& - \underbrace{\frac{\partial}{\partial \mathbf{u}_s}\left[\int_{\Omega_s} \left(\boldsymbol{\lambda}_1(\mathbf{x},0)\cdot\partial_t\mathbf{u}_s(\mathbf{x},0) - \rho_s\boldsymbol{\lambda}(\mathbf{x},0)\cdot\partial_t\mathbf{u}_s(\mathbf{x},0)\right)\mathrm{d}V\right]}_{③} \\
& + \underbrace{\frac{\partial}{\partial \mathbf{u}_s}\left[\int_{\Omega_s} \rho_s \partial_t\boldsymbol{\lambda}(\mathbf{x},T)\cdot\mathbf{u}_s(\mathbf{x},T)\,\mathrm{d}V\right]}_{④} - \underbrace{\frac{\partial}{\partial \mathbf{u}_s}\left[\int_{\Omega_s} \rho_s\boldsymbol{\lambda}(\mathbf{x},T)\cdot\partial_t\mathbf{u}_s(\mathbf{x},T)\,\mathrm{d}V\right]}_{⑤} \\
& + \underbrace{\frac{\partial}{\partial \mathbf{u}_s}\left[\int_0^T \int_{\Gamma_{fs}} \left(\boldsymbol{\sigma}_s(\mathbf{x},t)\cdot\mathbf{n}\cdot\boldsymbol{\lambda}(\mathbf{x},t) - \boldsymbol{\alpha}(\mathbf{x},t)\cdot\boldsymbol{\sigma}_s(\mathbf{x},t)\cdot\mathbf{n}\right)\mathrm{d}S\mathrm{d}t\right]}_{⑥} \\
& - \underbrace{\frac{\partial}{\partial \mathbf{u}_s}\left[\int_0^T \int_{\Gamma_{fs}} \left(\partial_{tt}\beta(\mathbf{x},t)\cdot\mathbf{u}_s(\mathbf{x},t)\cdot\mathbf{n} + \mathbf{T}(\mathbf{x},t)\cdot\mathbf{n}\cdot\mathbf{u}_s(\mathbf{x},t)\right)\mathrm{d}S\mathrm{d}t\right]}_{⑦} \\
= & \ 0.
\end{aligned} \tag{A10}$$

By zeroing ① to ⑦ simultaneously, we obtain the elastic adjoint-state equations

$$\begin{aligned}
& \rho_s \partial_{tt}\boldsymbol{\lambda}(\mathbf{x},t) - \nabla\cdot\mathbf{T}(\mathbf{x},t) = \sum\nolimits_{s,r} \beta_s \mathbf{S}_{s,r}^T \left(\mathbf{S}_{s,r}\mathbf{W}_{\mathbf{u}}(t) - \mathbf{d}_{\mathbf{u}}^{\text{obs}}(t)\right), \\
& \mathbf{T}(\mathbf{x},t) = \mathbf{C} : \nabla\boldsymbol{\lambda}(\mathbf{x},t), \\
& \boldsymbol{\lambda}_0(\mathbf{x},0) = -\rho_s\partial_t\boldsymbol{\lambda}(\mathbf{x},0), \quad \boldsymbol{\lambda}_1(\mathbf{x},0) = \rho_s\boldsymbol{\lambda}(\mathbf{x},0), \\
& \boldsymbol{\lambda}(\mathbf{x},T) = \mathbf{0}, \quad \boldsymbol{\partial}_t\boldsymbol{\lambda}(\mathbf{x},T) = \mathbf{0}, \\
& \boldsymbol{\alpha}(\mathbf{x},t)\cdot\mathbf{n} = \boldsymbol{\lambda}(\mathbf{x},t)\cdot\mathbf{n}, \quad \partial_{tt}\beta(\mathbf{x},t)\,\mathbf{n} = -\mathbf{T}(\mathbf{x},t)\cdot\mathbf{n}.
\end{aligned} \tag{A11}$$

A3 Acoustic–elastic coupled adjoint-state equation system

By combining equations in eqs (A6) and (A11) and eliminating $\beta(\mathbf{x},t)$ and $\boldsymbol{\alpha}(\mathbf{x},t)$, we get the acoustic–elastic coupled adjoint-state equation system

$$\begin{aligned}
& \tfrac{1}{\kappa}\partial_{tt}\mu^{(P)} - \nabla\cdot\left(\tfrac{1}{\rho_f}\nabla\mu^{(P)}\right) = \sum\nolimits_{s,r} \alpha_s \mathbf{S}_{s,r}^T \left(\mathbf{S}_{s,r}\mathbf{W}_P - \mathbf{d}_P^{\text{obs}}\right), && \text{in } \Omega_f, \\
& \rho_s\partial_{tt}\boldsymbol{\lambda} = \nabla\cdot\mathbf{T} + \sum\nolimits_{s,r} \beta_s \mathbf{S}_{s,r}^T \left(\mathbf{S}_{s,r}\mathbf{W}_{\mathbf{u}} - \mathbf{d}_{\mathbf{u}}^{\text{obs}}\right), \quad \mathbf{T} = \mathbf{C} : \nabla\boldsymbol{\lambda}, && \text{in } \Omega_s, \\
& \boldsymbol{\lambda}\cdot\mathbf{n} = \tfrac{1}{\rho_f}\nabla\mu^{(P)}\cdot\mathbf{n}, \qquad \mathbf{T}\cdot\mathbf{n} = \partial_{tt}\mu^{(P)}\mathbf{n}, && \text{on } \Gamma_{fs},
\end{aligned} \tag{A12}$$

and associated final conditions

$$\begin{aligned}
& \mu^{(P)}(\mathbf{x},T) = 0, \quad \partial_t\mu^{(P)}(\mathbf{x},T) = 0, \\
& \boldsymbol{\lambda}(\mathbf{x},T) = \mathbf{0}, \quad \boldsymbol{\partial}_t\boldsymbol{\lambda}(\mathbf{x},T) = \mathbf{0}.
\end{aligned} \tag{A13}$$